Results in Physics 26 (2021) 104343

Contents lists available at ScienceDirect

Results in Physics

journal homepage: www.elsevier.com/locate/rinp

Survey of optical and fluorescence traits of Tm^{3+}-doped alkali/mixed alkali oxides constituting B_2O_3-BaO-ZnO-LiF glasses for 0.45 μm laser and 1.46 μm fiber amplifier

G. Lakshminarayana [a,*], A.N. Meza-Rocha [b], O. Soriano-Romero [c], E.F. Huerta [d], U. Caldiño [d], A. Lira [e], Dong-Eun Lee [f,1,*], Jonghun Yoon [g,*], Taejoon Park [h,2,*]

[a] Intelligent Construction Automation Center, Kyungpook National University, 80, Daehak-ro, Buk-gu, Daegu 41566, Republic of Korea
[b] CONACYT-Benemérita Universidad Autónoma de Puebla. Postgrado en Física Aplicada. Facultad de Ciencias Físico-Matemáticas, Av. San Claudio y Av. 18, sur, Col. San Manuel Ciudad Universitaria, Puebla, Pue 72570, Mexico
[c] Posgrado en Física Aplicada, Facultad de Ciencias Físico-Matemáticas, Benemérita Universidad Autónoma de Puebla, Av. San Claudio y Av. 18 Sur, Col. San Manuel Ciudad Universitaria, Puebla, Pue 72570, Mexico
[d] Departamento de Física, Universidad Autónoma Metropolitana-Iztapalapa, P.O. Box 55-534, México, DF 09340, Mexico
[e] Departamento de Física, Facultad de Ciencias, Universidad Autónoma del Estado de México, C.P. 50000 Toluca, Mexico
[f] School of Architecture, Civil, Environment and Energy, Kyungpook National University, 1370, Sangyeok-dong, Buk-gu, DaeGu 702-701, Republic of Korea
[g] Department of Mechanical Engineering, BK21 FOUR ERICA-ACE Center, Hanyang University, 55, Hanyangdaehak-ro, Sangnok-gu, Ansan-si, Gyeonggi-do 15588, Republic of Korea
[h] Department of Robotics Engineering, Hanyang University, 55 Hanyangdaehak-ro, Ansan, Gyeonggi-do 15588, Republic of Korea

ARTICLE INFO

Keywords:
Borate glasses
Tm^{3+}
Judd-Ofelt analysis
Luminous efficiency of radiation
Blue laser
S-optical band amplifier

ABSTRACT

For six 1 mol% Tm^{3+}-doped B_2O_3-BaO-ZnO-LiF glasses containing single and mixed alkali oxides (fabricated by melt-cast approach), optical absorption, and visible and near-infrared (NIR) fluorescence features including visible luminescence decay times were explored. Optical band gaps, Urbach energy, and two-photon absorption coefficients were evaluated for all studied glasses. Judd–Ofelt (J–O) analysis from absorption spectra was performed to compute Tm^{3+}: 4f–4f transitions J–O parameters Ω_λ ($\lambda = 2, 4, 6$), and utilizing Ω_2, Ω_4 and Ω_6 values radiative transition probabilities (A_R), branching ratios (β_R), and radiative lifetimes (τ_R) for all Tm^{3+} ion's excited levels were assessed. For obtained intense blue emission band (454 nm) upon 358 nm excitation, various parameters considered in developing visible laser systems were calculated. Tm^{3+}: Na ions having sample exhibits high A_R, highest peak emission cross-section (σ^{em}_{max}) (=5.89 × 10^{-21} cm^2) and gain bandwidth(σ^{em}_{max} × $\Delta\lambda_{eff}$) (=9.69 × 10^{-27} cm^3) for $^1D_2 \rightarrow {}^3F_4$ luminescence transition in all glasses for a favorable blue lasing process. All emission decay curves of the $^1D_2$ upper level showed nonexponential nature. Commission Internationale de l'éclairage (CIE) coordinates, color purity, and luminous efficiency of radiation were derived from visible fluorescence spectra, and attained CIE (*x,y*) coordinates values reflect the purplish-blue light region. Under direct optical pumping of $^3H_6 \rightarrow {}^3H_4$ transition using 808 nm laser diode, NIR fluorescence spectra exhibit a wideband within 1.3–1.6 μm spectral range peaked at 1.46 μm ($^3H_4 \rightarrow {}^3F_4$ transition). NIR emissions effective bandwidth ($\Delta\lambda_{eff}$) was varied relying on different alkali oxides. $\Delta\lambda_{eff} \sim 121$ nm was deduced for Tm^{3+}: Li ions comprising glass with large σ^{em}_{max} (=1.832 × 10^{-21} cm^2), high(σ^{em}_{max} × $\Delta\lambda_{eff}$) (=2.22 × 10^{-26} cm^3), and optical gain (=12.608 × 10^{-25} cm^2s) for $^3H_4 \rightarrow {}^3F_4$ emission transition and its gain profile wraps the entire S-optical communication band range for efficient broadband amplification purpose in wavelength-division multiplexing systems.

* Corresponding authors.
E-mail addresses: gandham@knu.ac.kr (G. Lakshminarayana), dolee@knu.ac.kr (D.-E. Lee), yooncsmd@gmail.com (J. Yoon), taejoon@hanyang.ac.kr (T. Park).
[1] https://orcid.org/0000-0001-9205-3836
[2] https://orcid.org/0000-0002-7924-1776

https://doi.org/10.1016/j.rinp.2021.104343
Received 5 April 2021; Received in revised form 6 May 2021; Accepted 13 May 2021
Available online 21 May 2021

Introduction

Generally, glasses have favorable features like low cost, large versatility of compositions, easy fabrication techniques, and distinct shape and size productions (*e.g.* rods, discs, slabs, and thin films) than single crystals. Further, an occurrence of both wide absorption and emission bands inhomogeneously with adequate stimulated emission cross-sections (σ_{em}) and gain coefficients with rare-earth (RE) ions doping established glasses superiority over single crystals for their utilization in fiber optics and lasers since few decades onwards [1,2].

In all distinct trivalent RE ions, Tm^{3+} ($4f^{12}$) ion exhibits various near-infrared (NIR) and mid-infrared (MIR) emissions peaked at 0.8 μm ($^1G_4 \rightarrow {}^3H_5/{}^3H_4 \rightarrow {}^3H_6$), 1.2 μm ($^1G_4 \rightarrow {}^3H_4/{}^3H_5 \rightarrow {}^3H_6$), 1.47 μm ($^3H_4 \rightarrow {}^3F_4$), 1.9 μm ($^3F_4 \rightarrow {}^3H_6$), 2.3 μm ($^3H_4 \rightarrow {}^3H_5$), and 3.8 μm ($^3H_5 \rightarrow {}^3F_4$), and owing to these IR fluorescences, glasses incorporated with Tm^{3+} ion would have potential applications in wideband NIR light-sources (0.8 μm and 1.2 μm luminescences) [3], S+ (1.45–1.48 μm) and S-optical bands (1.48–1.53 μm) amplification (1.47 μm emission) [4,5], and defense, remote sensing, eye-safe LIDAR (light detection and ranging), and medicine (1.9 μm, 2.3 μm, and 3.8 μm fluorescences) [6–9]. Here the selection of host glass for lasing will relies on anticipated Tm^{3+}: NIR or MIR emission transitions upon suitable optical pumping. As Tm^{3+} ion shows intense absorption at ~ 800 nm ($^3H_6 \rightarrow {}^3H_4$) in doped materials, it could be efficiently pumped by employing commercially accessible 808 nm LDs (laser diodes) as usually RE^{3+} ions could be excited optically for wideband NIR or MIR emissions by ~ 0.98 μm or 0.808 μm LDs. Specifically, Tm^{3+}-doped fiber amplifier (TDFA) which possesses the capacity to amplify S-band WDM (wavelength-division multiplexing) signals, extend the bandwidths to lower wavelength side of C-band (1.53–1.57 μm) for which EDFAs (Er^{3+}-doped fiber amplifiers) are utilized nowadays commercially. TDFAs usually demonstrate larger pumping efficiency, enhanced bandwidth, cluster approach, and fewer nonlinear signal reduction than their competitors such as S-band FRAs (fiber Raman amplifiers) [10,11]. Here effective amplification could be achieved with Tm^{3+}: $^3H_4 \rightarrow {}^3F_4$ transition mostly in low phonon energy glasses which have minimal nonradiative (NR) multiphonon relaxations [12]. For WDM systems, ~1.47 μm peaked emission effective bandwidth ($\Delta\lambda_{eff}$) and levelness are vital to propagate a high number of optical signals and for avoiding the gain instability and cross-talk between channels [13]. Further, Tm^{3+} ion could exhibits up-conversion (UC) fluorescence in red ($^1G_4 \rightarrow {}^3F_4$ and $^3F_3 \rightarrow {}^3H_6$), blue ($^1D_2 \rightarrow {}^3F_4$ and $^1G_4 \rightarrow {}^3H_6$), ultraviolet ($^1I_6 \rightarrow {}^3F_4$ and $^1D_2 \rightarrow {}^3H_6$), and NIR ($^3H_4 \rightarrow {}^3H_6$) spectral regions under visible or NIR excitation wavelengths for color display, optical data storage, under sea-water optical transmission, visible laser, and biomedicine applications [14–17].

In recent past, Tm^{3+} ion's luminescence dynamics were detailedly inspected in various kinds of glass hosts such as phosphate [18], germanate [19], fluoride [20,21], tellurite [22,23], chalcogenide [24,25], silicate [26,27], and borate [28] glasses.

Though fluoride [14,20,29], tellurite [22,23,30], and chalcogenide [8,24,25] glasses are favorable for TDFAs because of their low phonon energies (fluorides ~ 500–600 cm^{-1}, tellurites ~ 700 cm^{-1}, and chalcogenides ~ 350–450 cm^{-1} [2]), problems like complicated synthesis approach, quick crystallization nature, and inadequate thermal and chemical stabilities are associated with them for viable uses. Further, ~1.47 μm NIR emission is difficult to obtain in Tm^{3+}: SiO_2-based glasses owing to NR multiphonon relaxations that suppress $^3H_4$ level decay time. Alternatively, Tm^{3+}-doped B_2O_3 glasses could be explored for NIR fiber lasers [28,31–33] because of their lower cost, vast glass-forming ability, high optical transparency, better thermal stability, good mechanical strength, and sufficient RE ion doping contents. Here to decrease B_2O_3 phonon energy ~ 1400 cm^{-1} and in turn to enhance RE ion radiative emissions efficiency distinct metal fluorides (*e.g.* alkali/alkaline/heavy metal) should be included in the matrix [34,35], as oxyfluoride glasses possess merits of both oxide and fluoride compounds in which fluorine ions could alter RE ion local ligand field and lower the OH^- groups and also extend IR cut-off edges to longer wavelength side [34–38]. As a modifier in glass, BaO does not contribute to network formation and causes an improvement in the thermal stability of glass [39]. ZnO (E_g = 3.37 eV) acts as a network former (ZnO_4 units) or modifier resting on its included content (high or low) as a glass constituent, and Masuda et al. [40] examined the thermal features and ZnO anomaly for B_2O_3–BaO–ZnO glass system fabricated with low-melting points. Moreover, ZnO addition enhances both glass-forming ranges and refractive index. Likewise, as modifiers, Li_2O or Na_2O, or K_2O generates non-bridging oxygens (NBOs) through BO_3 to BO_4 unit modification and decreases melting points of glass [41].

Table 1
Nominal chemical composition of the synthesized glasses (mol %).

Sample code	B_2O_3	BaO	ZnO	LiF	Li_2O	Na_2O	K_2O	Tm_2O_3
A	49	10	10	10	20	0	0	1.0
B	49	10	10	10	0	20	0	1.0
C	49	10	10	10	0	0	20	1.0
D	49	10	10	10	10	10	0	1.0
E	49	10	10	10	0	10	10	1.0
F	49	10	10	10	10	0	10	1.0

Regarding distinct light sources, CP (color purity) (from CIE (Commission Internationale de l'éclairage) chromaticity coordinates) and LER (luminous efficacy of radiation) are necessary aspects apart from CCT (correlated color temperature) and CRI (color rendering index) to assess the emitted light quality [42,43].

In current work, for 1 mol% Tm^{3+}-doped borate-rich glasses containing single and mixed alkali oxides, we investigated visible and NIR fluorescence characteristics for blue laser and S-optical band amplification applications. Visible emissions and Tm^{3+}: $^1D_2$ level decay lifetimes were acquired upon UV light excitation. NIR luminescence was achieved by 808 nm LD pumping. All samples show intense luminescences peaked at 0.454 μm and 1.463 μm. Optical band gaps, Urbach energies (ΔE), Judd–Ofelt (J–O) parameters, and radiative parameters (radiative transition probabilities (A_R), radiative lifetimes (τ_R), and branching ratios (β_R) of emitting levels of Tm^{3+} ion) were computed following relevant absorption and emission spectra. CIE chromaticity coordinates, CP, and LER were derived from visible fluorescence spectra for all examined samples and discussed. Further σ^{em}_{max} and $\Delta\lambda_{eff}$ were determined for $^1D_2 \rightarrow {}^3F_4$ and $^3H_4 \rightarrow {}^3F_4$ transitions from emission spectra.

Experimental

Synthesis

Six Tm^{3+}-doped B_2O_3-rich glasses with constituents of 49 B_2O_3–10 BaO–10 ZnO–10 LiF–*x* Li_2O–*y* Na_2O–*z* K_2O–1.0 Tm_2O_3 (mol %) (where $x = 20, y = 0, z = 0$; $x = 0, y = 20, z = 0$; $x = 0, y = 0, z = 20$; $x = 10, y = 10, z = 0$; $x = 0, y = 10, z = 10$ and $x = 10, y = 0, z = 10$) (see Table 1) have been fabricated by a customary melting-and-quenching approach in air atmosphere. B_2O_3 (99.98%), $BaCO_3$ (99.98%), ZnO (99.99%), anhydrous LiF (≥99.99%), Li_2CO_3 (99.99%), Na_2CO_3 (≥99.5%), K_2CO_3 (≥99%), and Tm_2O_3 (99.99%) chemicals all procured from Sigma-Aldrich were used as collected for glass preparation. Here exact amounts of $BaCO_3$, Li_2CO_3, Na_2CO_3, and K_2CO_3 (carbonate compounds) were utilized with gravimetric factors of 1.287, 2.473, 1.71, and 1.467 accordingly for BaO, Li_2O, Na_2O, and K_2O oxides. As presented in Table 1, synthesized all six glasses were identified as 'A', 'B', 'C', 'D', 'E', and 'F' sequentially for ease of use. First, conditional on the respective sample's composition (molar ratio), initial raw materials for a 20 g batch were precisely weighed utilizing a high-precision digital balance, and then carefully well-mixed and ground evenly by an agate mortar and pestle for 1 h. Next, obtained each glass uniformly mixed powders were collected in high-purity alumina crucibles with lids and heated for 30 min at 950 °C in a high-temperature electric furnace to attain molten

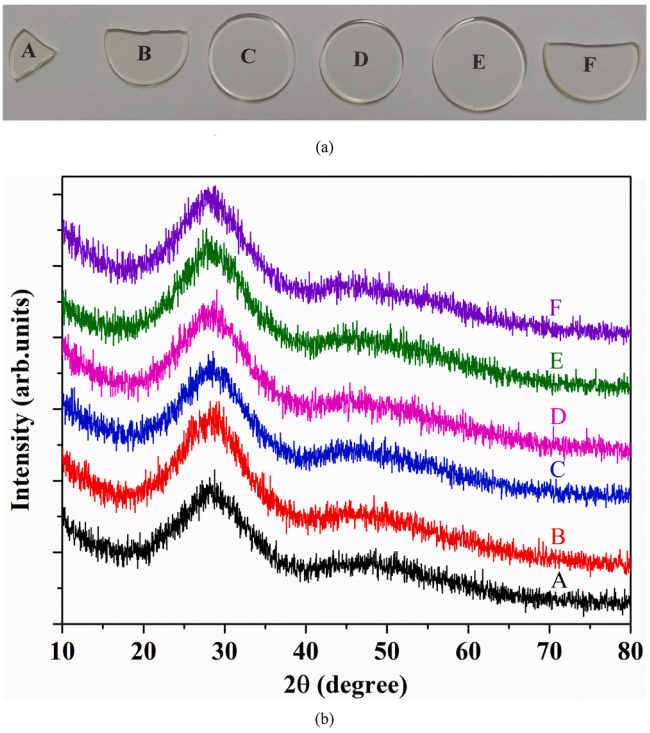

Fig. 1. (a) Photograph of all the studied glasses (b) X-ray diffraction (XRD) profiles of all the prepared glasses.

liquids. To acquire high homogeneity liquids with complete mixing and to remove the existence of bubbles, molten liquids were frequently stirred at the time of heating. Then these molten liquids were rapidly poured onto stainless-steel plates and pressed by another stainless-steel plate to get optically transparent bulk glasses with diameter ~ 3–4 cm and ~ 0.5 cm uniform thickness. Here no apparent defects like phase separations or cracks have been noticed in any sample. Later, to ease the thermal strain and to minimize the mechanical stress accompanied with non-uniform quick quenching action, these as-prepared glasses were immediately annealed at 350 °C for 5 h in a muffle furnace before it is switched off. In the end, all samples were allowed to cool steadily in the furnace to ambient temperature. For optical absorption and fluorescence aspects study, all annealed A–F samples were cut and polished on both sides to obtain good optical quality, and a small portion of each glass was pulverized separately for X-ray diffraction (XRD) study. Fig. 1(a) shows a photograph of all polished A–F glasses to 1.5 mm thickness.

Measurements

For all A–F glasses, physical characteristics such as thickness, refractive index (error: ± 0.001), and hydrostatic density (accuracy of ± 0.001 g/cm^3) were measured utilizing a digital Vernier caliper gauge, employing an Abbe refractometer at 589.3 nm (sodium vapor lamp) wavelength with 1-Bromonaphthalene as contact liquid, and by the Archimedes's principle using a microbalance with xylene (99.99%) as an immersion fluid, accordingly. Each sample was tested three times. XRD studies have been performed on all powdered A–F samples within 10°–80° (2θ) range at 2°/min scanning rate utilizing an Ital Structure APD 2000 diffractometer with Cu-K$_\alpha$ ($\lambda = 1.5418$ Å) radiation where *X*-ray tube was operated at 20 mA anode current and 40 kV voltage, and by a scintillation detector scattered *X*-rays intensity was recorded. Optical absorption spectra of all A–F samples were registered using UV–Vis-NIR Varian Cary 5000 spectrophotometer covering 200–2000 nm wavelength range with a spectral resolution ~ 1 nm. Here absorption coefficient $\alpha(\lambda)$ was computed as $\alpha(\lambda) = 2.303 \times A/t$ (A = absorbance, t = thickness (cm)). For all A–F samples, utilizing Horiba Jobin–Yvon Fluorolog 3–22 spectrofluorometer supplied with an R928P Hamamatsu PMT detector and a 450 W ozone-free CW Xe lamp as pump source, in steady-state mode visible luminescence and excitation spectra (spectral resolution 0.5 nm, entrance and exit slits width ~ 1.5 mm) were recorded, and the same setup with a flash Xe lamp was employed for Tm^{3+}: $^1D_2 \rightarrow {}^3F_4$ transition fluorescence decay time measurements in phosphorescence mode. The decay patterns were collected at 0.01 ms delay time, 3 μs half-width pumping pulse, and 5 ms sample window. NIR emission spectra at 1300–1600 nm spectral range have been measured by an FLS1000 fluorescence spectrometer (Edinburgh Instruments, UK) upon 808 nm pulsed diode laser pumping (direct excitation from Tm^{3+}: $^3H_6$ level to $^3H_4$ state) and furnished with a NIR-PMT (InGaAs) detector. At ambient temperature, all mentioned measurements were carried out and for luminescence (visible and NIR) investigations, to derive comparable outcomes among all A–F glasses we kept experimental settings (*i.e.* sample shape, position, incident pumping light angle) the same. CIE chromaticity color coordinates were calculated from the measured visible luminescence spectra of all A–F glasses.

Results and discussion

X-ray diffraction (XRD) analysis

Within $10° \leq 2\theta \leq 80°$ range XRD profiles of all A–F glasses are displayed in Fig. 1(b). Being identical all XRD curves reveals no discrete or sharp peaks particularly, but only two wide-ranging diffuse bands at $2\theta = 19°–39°$ and 39°–62°, representative of a non-crystalline state. This affirms all A–F samples' fully amorphous phase with short-range structural order or long-range disorder of atoms arrangement in them.

Optical absorption spectra and J–O analyses

In a glass matrix, usually, RE ion's optical absorption features rely on RE ion's local environment and RE ion connection with ligands. Fig. 2(a) illustrates absorption spectra (y-axis scale in absorption coefficient (cm^{-1})) of all A–F glasses within 280–2000 nm wavelength range. Seven inhomogeneously wide discrete absorption bands peaked at 358 nm, 465 nm, 657 nm, 685 nm, 791 nm, 1208 nm, and 1657 nm attributable to transitions originating from Tm^{3+}: $^3H_6$ ground state to corresponding $^1D_2$, $^1G_4$, $^3F_2$, $^3F_3$, $^3H_4$, $^3H_5$, and $^3F_4$ upper levels ($4f^2$–$4f^2$ intra-configurational) [18,36] are identified from Fig. 2(a). Here for all A–F samples noticed absorption peak positions and shape are the same, possibly owing to the similar ligand field, hinting on Tm^{3+} ions uniform statistical distribution. In all transitions, only $^3H_6 \rightarrow {}^3H_5$ IR transition holds both magnetic-dipole and electric-dipole (MD and ED) interaction contributions and all remaining are only ED in character. Further, $^3H_6 \rightarrow {}^3F_4$ is classified as "hypersensitive" transition (obey $\Delta S = 0$, $|\Delta L| \leq 2$ and $|\Delta J| \leq 2$ selection rules [44]) as its intensity varies dramatically resting on Tm^{3+} ion neighboring environment in a host matrix. An intense absorption band centered at 791 nm and wide absorption band peaked at 1657 nm signifies that all A–F samples could be excited effectively utilizing pump sources such as high power AlGaAs LDs or Ti: Sapphire lasers available commercially and ~ 1.5 μm fiber laser. UV absorption spectra at 250–300 nm wavelength range for all A–F samples are displayed in Fig. 2(b). Considering the steep rise in absorption after $^1D_2$ higher state at lower spectral region (*i.e.* < 342 nm) (see Fig. 2(a)), noticed three strong and wide CT (charge-transfer) bands centered at 260 nm, 275 nm, and 288 nm from Fig. 2(b) could be originated because of unavoidable trace impurities such as Fe^{3+} ion related electron transfer processes. These trace impurities may be presented (even at ppm level) in the selected initial raw chemicals utilized for all A–F samples' fabrication. Earlier such UV absorption bands were also identified in NdF_3-doped oxyfluoride lithium borate [45] and P_2O_5-B_2O_3-Na_2O-NdF_3 [46] glasses by other researchers and ascribed similarly. Commonly, in highly UV transparent Tm^{3+}: crystals owing to $^3H_6 \rightarrow {}^3P_2$, $^3H_6 \rightarrow {}^3P_1$, and

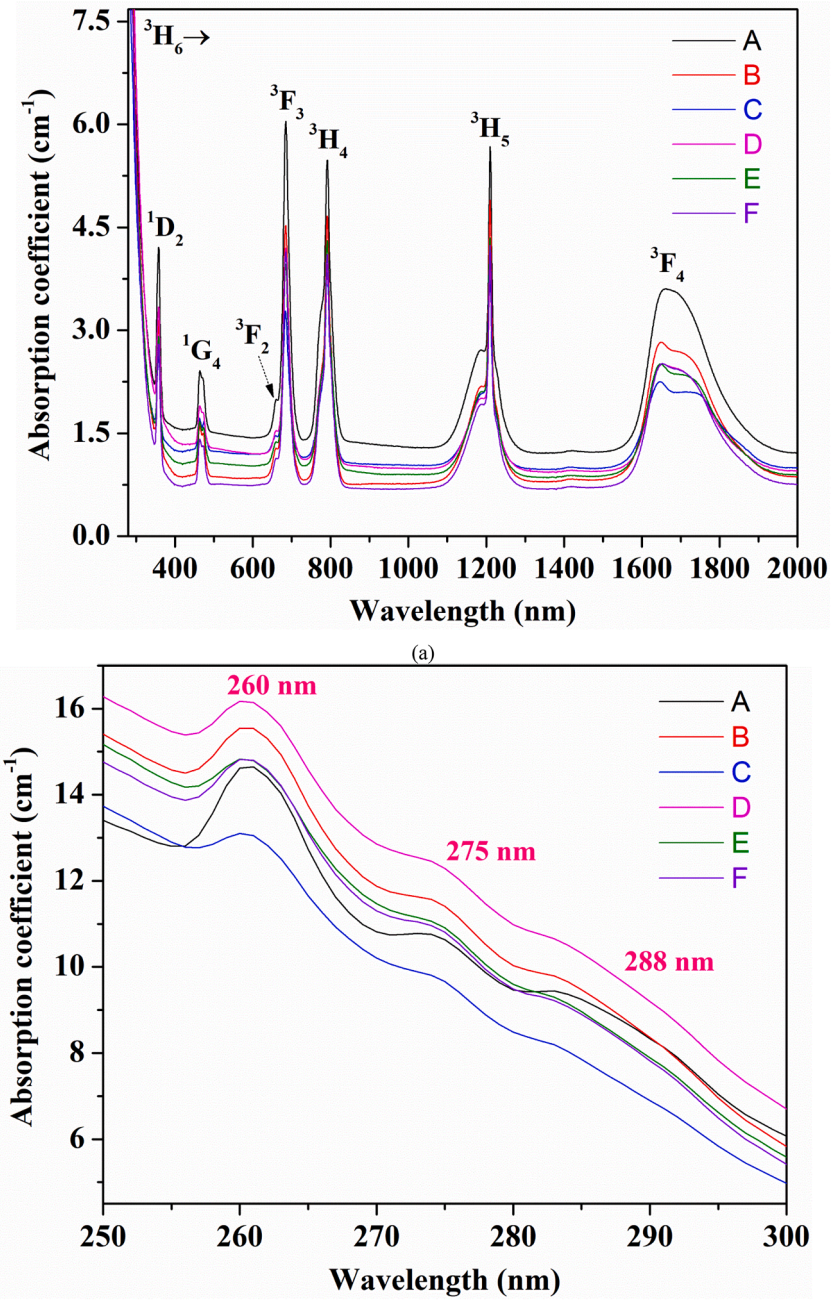

Fig. 2. (a) UV–Vis-NIR optical absorption spectra (b) UV absorption spectra at 250–300 nm wavelength range for all 1.0 mol% Tm^{3+}-doped glasses. Here, the y-axis scale is shown in the absorption coefficient (cm^{-1}) values.

$^3H_6 \rightarrow {}^3P_0 + {}^1I_6$ transitions mentioned three UV absorption bands could be observed [47].

Fig. 3(a) shows UV absorption spectra within 290–390 nm wavelength range used for cutoff wavelength or fundamental absorption edge ($\lambda_{cut\text{-}off}$ or λ_{edge}) estimation for all A–F samples. Generally, λ_{edge} is connected with a glass matrix structure itself, and for all A–F glasses as a characteristic of them, λ_{edges} are not sharply defined. Following Ref. [48], evaluated λ_{edge} (error± 0.5 nm) values are given in Table 2 along with measured density and refractive index values. From Table 2 it can be seen that λ_{edge} value changes to shorter wavelength side from 341.65 nm to 323.64 nm for A–C samples while for D–F glasses it decreases in the order D > E > F. Overall, λ_{edge} value varies at 341.65 – 323.64 nm range. Such deviations or reductions in λ_{edge} with distinct Li, Na, K, Li-Na, Na-K, and Li-K ions' existence from A to F glass hints on the BO (bridging oxygen) bonds density variation (NBOs occurrence) in studied glasses as λ_{edge} relies on 'O' (Oxygen) bond strength in B_2O_3 network. Here glass C could be utilized for the UV cutoff goal in all samples. It is widely known that for insulators or semiconductors, the band gap represents the energy break from conduction band edge to valance band maximal. Following UV absorption spectra, for all A–F samples, considering Mott and Davis [49] or Tauc [50] proposed models, optical band gap (E_{opt}) is determined using the below relation between 'α' and E_{opt} [49]:

$$\alpha(v) = B \times \frac{(hv - E_{opt})^r}{hv} \quad (1)$$

where B (band-tailing parameter) = constant, $h\nu$ = photon energy, and

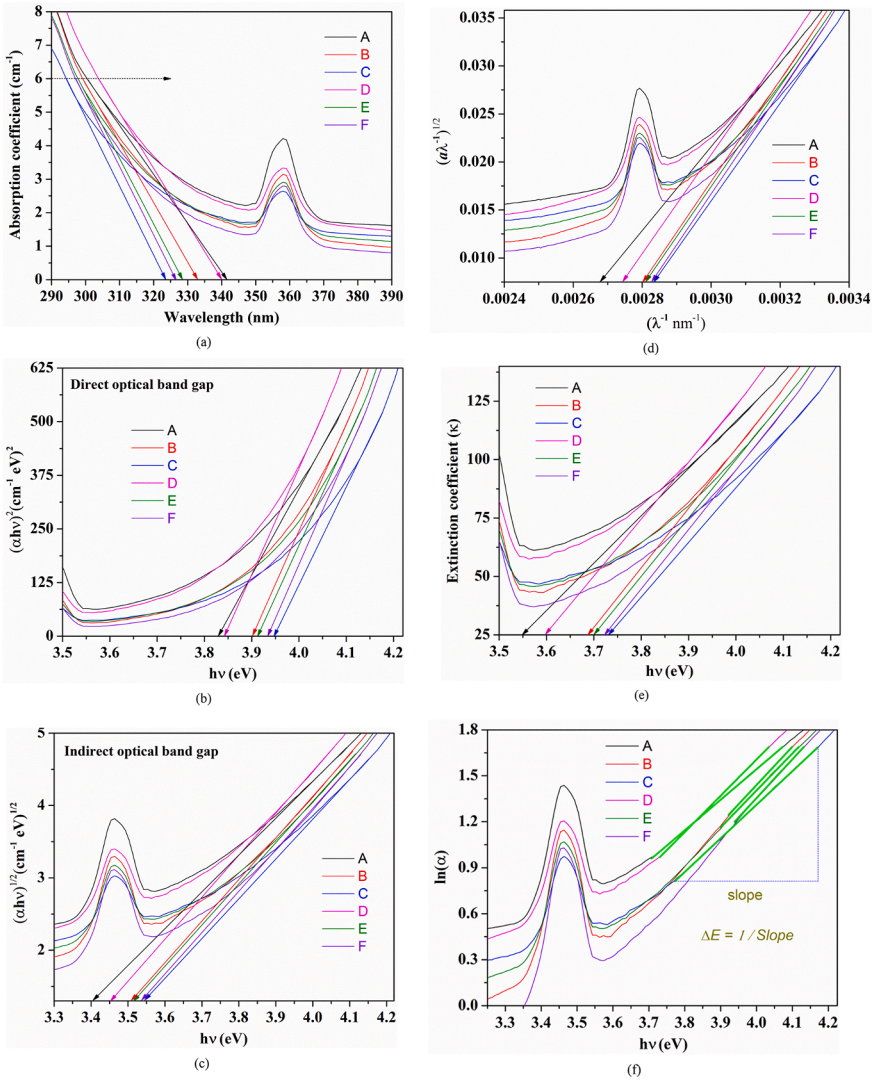

Fig. 3. (a) UV optical absorption spectra of all the prepared glasses. Here, the straight lines drawn onto *X*-axis indicate the $\lambda_{cut\text{-}off}$ wavelengths for the respective glasses. Plots of (b) $(\alpha h\nu)^2$ vs. $(h\nu)$ for direct optical band gap (c) $(\alpha h\nu)^{1/2}$ vs. $(h\nu)$ for indirect optical band gap (d) $(a\lambda^{-1})^{1/2}$ vs. (λ^{-1}) for optical band gap (E_{opt}^{asf}) (e) extinction coefficient (κ) vs. $h\nu$, and (f) Urbach's plots for all the studied glasses. In Fig. 3 (b-e), the lines drawn onto *X*-axis indicate the respective optical band gap energies of the studied glasses.

Table 2
The fundamental absorption edge ($\lambda_{edge} \pm 0.5$ nm), direct optical band gap ($E_{opt} \pm 0.01$ eV), indirect optical band gap ($E_{opt} \pm 0.01$ eV), optical band gap data evaluated through ASF method ($E_{opt}^{asf} \pm 0.01$ eV), optical band gap from the extinction coefficient (E_{opt} from 'κ' ± 0.01 eV), Urbach energy ($\Delta E \pm 0.002$ eV), two photon absorption coefficient ($\beta \pm 0.01$ cm/GW), density (±0.001 g/cm^3), and refractive index (±0.001) of all the studied A–F glasses.

Sample code	λ_{edge} (nm)	Direct optical band gap, E_{opt} (eV)	Indirect optical band gap, E_{opt} (eV)	$(1/\lambda_g)$ ($\pm 1 \times 10^{-6}$ nm^{-1})	λ_g ($\pm 1 \times 10^{-6}$ nm)	Optical band gap, E_{opt}^{asf} (eV)	E_{opt} from 'κ' (eV)	Urbach Energy, ΔE (eV)	β (cm/GW)	Density (g/cm^3)	Refractive index
A	341.65	3.829	3.406	0.00268	373.1343	3.323	3.550	0.508	9.17	2.951	1.665
B	333	3.902	3.507	0.00280	357.1428	3.472	3.686	0.400	8.35	3.013	1.673
C	323.64	3.947	3.544	0.00283	353.3569	3.509	3.731	0.454	8.05	3.032	1.689
D	340	3.842	3.452	0.00274	364.9635	3.398	3.598	0.425	8.80	2.945	1.676
E	328.59	3.912	3.514	0.00281	355.8719	3.484	3.700	0.413	8.30	3.025	1.683
F	326.73	3.933	3.536	0.00282	354.6099	3.497	3.723	0.390	8.12	2.949	1.681

index, $r = 1/2$ and 2 for direct and indirect transitions accordingly.

Fig. 3(b) and (c) depict Tauc plots for direct and indirect transitions correspondingly for all A–F glasses. Here E_{opt} is evaluated by projecting the linear regions to $(\alpha h\nu)^2 = 0$ and $(\alpha h\nu)^{1/2} = 0$ accordingly, and the derived values (error ±0.01 eV) are listed in Table 2. From Table 2 one can see that the values of E_{opt} (direct) > E_{opt} (indirect) for all A–F samples as E_{opt} (direct) profiles fit falls on the greater energy region. Both direct and indirect E_{opt} values increase from A to C glass and for mixed alkali oxides constituting samples in D < E < F order, indicating structural changes activity in these glasses, *i.e.* fewer NBOs formation in preference to BOs, as generally in amorphous substances like glasses, E_{opt} increases owing to NBO ions reduction. E_{opt} shift to larger energies from A to C glass and D to F sample discloses the increasing network cross-linking with a lesser degree of disorder in them [41]. As the indirect transition is located at smaller energy than the direct one, all A–F glasses are non-direct or indirect materials.

Further, applying the ASF (absorption spectrum fitting) procedure proposed by Escobar-Alarcon et al. [51] and Souri and Shomalian [52] in which E_{opt} could be computed without a thin film or glass thickness requirement but only from absorption spectra, for all A–F samples E_{opt} is

Table 3
Absorption band assignments (from the ground state, $^3H_6$), experimental (f_{exp}) and calculated (f_{cal}) oscillator strengths ($\times 10^{-6}$) of all the 1.0 mol% Tm^{3+} -doped glasses along with J–O parameters. Wavelengths correspond to average transition energies.

Glass code			A		B		C		D		E		F	
Transition		λ (nm)	f_{exp}	f_{cal}	f_{exp}	f_{cal}	f_{exp}	f_{cal}	f_{exp}	f_{cal}	f_{exp}	f_{cal}	f_{exp}	f_{cal}
$^3H_6$→														
	$^1D_2$	358	7.30	6.65	6.09	5.32	3.87	3.16	4.96	4.37	5.10	4.16	5.84	5.08
	$^1G_4$	468	3.34	2.31	3.18	2.16	2.46	1.57	2.44	1.62	2.79	1.84	2.89	1.99
	$^3F_2$	660	0.67	1.90	0.61	1.77	0.47	1.32	0.50	1.39	1.04	1.61	0.51	1.63
	$^3F_3$	685	8.35	8.85	6.96	7.76	4.36	5.34	5.70	6.19	5.75	6.74	6.57	7.23
	$^3H_4$	789	8.44	8.28	8.11	8.09	6.08	6.22	6.14	6.04	7.22	7.28	7.47	7.37
	$^3H_5$	1194	5.39	4.83	5.32	4.45	4.26	3.23	3.96	3.44	4.83	3.92	4.81	4.10
			4.09 ed		4.00 ed		2.90 ed		2.63 ed		3.49 ed		3.47 ed	
			1.30md[a]		1.32md[a]		1.36md[a]		1.33md[a]		1.34md[a]		1.34md[a]	
	$^3F_4$	1711	6.65	6.80	6.26	6.43	4.58	4.73	4.68	4.81	5.37	5.52	5.75	5.90
RMS deviation (× 10–^{6})			0.507		0.508		0.455		0.427		0.468		0.484	
J – *O* parameters (× 10^{-20} cm^2)														
Ω_2			8.992 ± 0.231		9.649 ± 0.674		7.966 ± 0.723		6.718 ± 0.332		8.746 ± 0.922		8.585 ± 0.487	
Ω_4			4.947 ± 0.305		3.789 ± 0.602		2.062 ± 0.587		3.142 ± 0.351		2.792 ± 0.797		3.630 ± 0.474	
Ω_6			3.824 ± 0.451		3.535 ± 0.586		2.588 ± 0.693		2.765 ± 0.384		3.219 ± 0.572		3.224 ± 0.505	

[a] Magnetic dipole (md) oscillator strength was subracted from experimental oscillator strength for J–O analysis

determined from the equation:

$$E_{opt}^{asf} = \frac{1240}{\lambda_g} \quad (2)$$

where λ_g = wavelength linked to E_{opt}.

Fig. 3(d) exhibits the plots of $(a\lambda^{-1})^{1/2}$ vs (λ^{-1}) (a = absorbance) for (E_{opt}^{asf}) estimation at $(a/\lambda)^{1/2} = 0$ with curves linear region extrapolation, and acquired $1/\lambda_g$, λ_g, and (E_{opt}^{asf}) (eV) values for all A–F glasses utilizing ASF approach are presented in Table 2. Here E_{opt}^{asf}values (alters at 3.323 (lowest) –3.509 eV (highest) range) show an identical trend as direct and indirect E_{opt} values for all alkali and mixed alkali oxides comprising samples, and they closely match with indirect E_{opt} values.

Later, adopting the relation between 'α' and 'κ' (extinction coefficient) as [53]:

$\alpha = \frac{4\pi\kappa}{\lambda}$ (3)for all A–F samples, E_{opt} (experimental) is evaluated by drawing the linear parts to 'κ' = 0. Fig. 3(e) illustrates the plots of 'κ' against $h\nu$ for all A–F glasses and obtained E_{opt} values are tabulated in Table 2. E_{opt} from 'κ' values for all A–F glasses also exhibits a similar course as direct and indirect E_{opt} value and it is related closely with Mott–Davis equation for $r = 2$ transition for sample A while its values fall almost in between for $r = 1/2$ and 2 transitions for rest of the glasses. Here E_{opt} (experimental) deviates at 3.55–3.731 eV range for all studied glasses.

For many non-crystalline semiconductors, at optical absorption edge, 'α' raises exponentially with $h\nu$ and adheres to the Urbach rule [54] as:

$$\alpha(\nu) = \alpha_0 \exp\left(\frac{h\nu}{\Delta E}\right) \quad (4)$$

(or)

$$\ln\alpha(\nu) = (h\nu/\Delta E) + \text{constant} \quad (5)$$

where α_0 = constant, ΔE = Urbach energy.

ΔE characterizes the band tails width of localized states in the band gap. This means it's a transition involving localized tail states next to valance band and conduction band that stretches into band gap. Here ΔE could be calculated from the inverse of the slopes of the linear portions of ln(α) vs $h\nu$. Fig. 3(f) displays Urbach's plots for all A–F glasses and derived ΔE values (error ±0.002) are given in Table 2. In Li, Na, and K ions having samples, glass B possesses the lowest ΔE (0.4 eV) whereas for mixed alkali oxides constituting glasses ΔE values vary inversely with E_{opt} where sample F has the minimum ΔE (0.39 eV). Minimal ΔE values reflect usually the least localized states tails width into band gap and feasibility of minimal defects in glasses. In all samples, the highest ΔE (0.508 eV) value of glass A indicates its larger propensity to transform weak bonds into defects. Overall, all A–F samples have larger ΔE values (0.39–0.508 eV range) as opposed to crystalline substances related values (ΔE = 0.046–0.066 eV) [49].

For alkali or TM (transition metal) oxides comprising glasses, M. Abdel-Baki et al. [55] have derived a linear relation between E_{opt} and TPA (two-photon absorption) coefficient (β) as:

β (cm/GW) = 36.76 – 8.1 E_{opt} (eV) (6) Using Eq. (6), for all A–F samples applying E_{opt} (indirect) values, obtained β values are listed in Table 2. β value varied within 9.17–8.05 cm/GW range in all investigated glasses. Since for all-optical switching waveguides device operation TPA is a crucial limiting factor [56], a minimal β (8.05 cm/GW) possessing glass C could be desirable for this aim. So by altering the E_{opt} one can easily control the TPA for a specific set of materials. Commonly, acidic (B_2O_3) and basic (alkali metal or ZnO) oxides combination in glass gives a lower TPA than alone acidic oxides [55].

Additionally, for all A–F glasses, utilizing all observed absorption transitions, f_{exp}, Judd–Ofelt (J–O) parameters (Ω_2, Ω_4, and Ω_6), f_{cal}, and δ_{rms} (root-mean-square error) deviations for f_{exp} and f_{cal} are computed employing J–O model [57,58], and attained results are presented in Table 3. For related operated well-known formulae one could refer to Refs. [28,31,32,36,57,58]. MD term arises for transitions which follow $\Delta J = 0, \pm 1$ and $\Delta S = \Delta L = 0$ rules and does not rely on ligand fields though usually RE ions f–f transitions (parity forbidden) intensity depends. Here derived smaller δ_{rms} values signifies the reliability of the J–O model calculation approach. The uncertainties associated with the J–O parameters were obtained directly from the J–O fit considering residual amounts between calculated and experimental absorption intensities. From Table 3 data, it is obvious that samples A, B, D, and F show $\Omega_2 > \Omega_4 > \Omega_6$ trend while $\Omega_2 > \Omega_6 > \Omega_4$ and $\Omega_2 > \Omega_6 > \Omega_4$ courses are obtained for C and E glasses correspondingly. Here Ω_4 is highly reliant on U^4 reduced matrix element and frequently has fewer quantities than U^2 & U^6 owing to Tm^{3+} neighboring locality non-symmetry. Commonly, parameters Ω_2, Ω_4, and Ω_6 reflect the bonding nature between RE ions and ligand anions, and the localized structure surrounding RE ions sites. Specifically, Ω_2 corresponds to both local field symmetry around RE ions and RE ions and anions chemical bonds covalence in glass, whereas Ω_6 indicates RE ions and associated anions ionic bonding character and could be varied by glass composition [59].

Ω_4 specifies bulk (degree of viscosity and rigidity) characteristics [32]. Here the larger Ω_2 value for sample B in all glasses reveals lower symmetry at Tm^{3+} ion sites locality and high covalency between Tm^{3+}

Table 4
Comparison of Judd–Ofelt intensity parameters (Ω_λ, $\times 10^{-20}$ cm^2) and their trend of glass D with different Tm^{3+} -doped glass systems.

Glass system	Ω_2	Ω_4	Ω_6	Trends of Ω_λ	Reference
Glass D	6.718	3.142	2.765	$\Omega_2 > \Omega_4 > \Omega_6$	Present work
BGGN1.0T glass	4.34	1.85	1.49	$\Omega_2 > \Omega_4 > \Omega_6$	[60]
BBLC 1.0Tm glass	0.5803	0.2033	0.1678	$\Omega_2 > \Omega_4 > \Omega_6$	[61]
$36Bi_2O_3$–$54GeO_2$-$10Na_2O$-$1Tm_2O_3$ glass	4.55	0.82	1.16	$\Omega_2 > \Omega_6 > \Omega_4$	[62]
PPbKANTm1.0 glass	7.81	0.95	0.55	$\Omega_2 > \Omega_4 > \Omega_6$	[63]
$50ZrF_4$·$33BaF_2$·$12AlF_3$·$5YF_3$·$1.0TmF_3$ glass	3.16	1.10	1.31	$\Omega_2 > \Omega_6 > \Omega_4$	[64]
ZBLAN: Tm^{3+} glass	2.31	1.28	1.17	$\Omega_2 > \Omega_4 > \Omega_6$	[65]
$60TeO_2$-$25ZnO$-$9Na_2CO_3$-$5TiO_2$-$1Tm_2O_3$ glass	8.88	1.34	1.91	$\Omega_2 > \Omega_6 > \Omega_4$	[66]
$80GeO_2$–$8Ga_2O_3$–$10BaO$-$2Nb_2O_5$–$6PbO$-$1Tm_2O_3$ glass	5.66	1.36	1.08	$\Omega_2 > \Omega_4 > \Omega_6$	[67]
TeNbK1.0Tm glass	4.51	0.76	1.13	$\Omega_2 > \Omega_6 > \Omega_4$	[68]
KCaAlP:$0.75Tm^{3+}$ glass	5.63	1.75	1.11	$\Omega_2 > \Omega_4 > \Omega_6$	[69]
$61.5P_2O_5 + 10K_2O + 15.5SrO + 12Al_2O_3 + 1Tm_2O_3$ glass	8.37	1.08	3.22	$\Omega_2 > \Omega_6 > \Omega_4$	[70]

Table 5
Emission transitions (SLJ → S′L′J′), wavelengths (λ_{em}, nm), electric (A_{ed}, s^{-1}), magnetic (A_{md}, s^{-1}), and total radiative transition probabilities (A_R, s^{-1}), branching ratios (β_R), and radiative (τ_{rad}, μs) lifetimes of glass B. Measured lifetime (τ_{meas}, μs) and quantum yield (η, %) of $^1D_2$ higher energy level are also included.

Transition			λ_{em}	A_{ed}	A_{md}	A_R	β_R	τ_{rad}	τ_{meas}
$^1D_2$	→	$^1G_4$	1506[b]	162		162	0.0077	47.50	21.24
		$^3F_2$	786	1235		1235	0.0587		
		$^3F_3$	750	2980		2980	0.1416		
		$^3H_4$	658[b]	4549		4549	0.2161		
		$^3H_5$	514[a]	113		113	0.0054		
		$^3F_4$	454[a]	4825		4825	0.2292		
		$^3H_6$	358	7187		7187	0.3413		
						$\eta(\%)\,^1D_2 \rightarrow {}^3F_4$		44.7	
$^1G_4$	→	$^3F_2$	1616	14		14	0.0046	334.80	
		$^3F_3$	1474	56		56	0.0188		
		$^3H_4$	1149	29		29	0.0098		
		$^3H_5$	770	715		715	0.2392		
		$^3F_4$	650[a]	1289		1289	0.4315		
		$^3H_6$	479[a]	884		884	0.2961		
$^3F_2$	→	$^3F_3$	16,703	0	2	2	0.0010	625.54	
		$^3H_4$	3980	12		12	0.0074		
		$^3H_5$	1469	220		220	0.1378		
		$^3F_4$	1071	657		657	0.4110		
		$^3H_6$	659	708		708	0.4428		
$^3F_3$	→	$^3H_4$	5225	1		1	0.0002	335.18	
		$^3H_5$	1611	279		279	0.0935		
		$^3F_4$	1144	318	341	659	0.2210		
		$^3H_6$	686	2045		2045	0.6853		
$^3H_4$	→	$^3H_5$	2329	44	114	158	0.1115	703.73	
		$^3F_4$	1463[a]	98		98	0.0691		
		$^3H_6$	808[a]	1164		1164	0.8194		
$^3H_5$	→	$^3F_4$	3949	3		3	0.0059	1857.34	
		$^3H_6$	1193	246	289	535	0.9941		
$^3F_4$	→	$^3H_6$	1821[b]	175		175	1.0000	5704.74	

[a] Experimental data [b] Calculated values from emission spectrum

ions and ligand anions when Na_2O was incorporated. Both Ω_4 and Ω_6 are the minimal for glass C (K_2O added one) where Ω_6 is vibronic dependent and reduces with rigidity improvement in a medium's environment around RE ion.

Table 4 shows J–O parameters and their trend derived for sample D compared to distinct other Tm^{3+}-doped glass systems [60–70]. Here we choose glass D for comparison as it exhibits relatively higher visible fluorescences intensity (discussed in 3.3 section) in all examined samples. From Table 4, Ω_2 value for glass D is found to be higher than BGGN1.0T [60], BBLC 1.0Tm [61], $36Bi_2O_3$–$54GeO_2$-$10Na_2O$-$1Tm_2O_3$ [62], $50ZrF_4$ ·$33BaF_2$ ·$12AlF_3$· $5YF_3$·$1.0TmF_3$ [64], ZBLAN: Tm^{3+} [65], $80GeO_2$–$8Ga_2O_3$–$10BaO$-$2Nb_2O_5$–$6PbO$-$1Tm_2O_3$ [67], TeNbK1.0Tm [68], and KCaAlP:$0.75Tm^{3+}$ [69] glasses respective values. Moreover, for sample D obtained Ω_2, Ω_4, and Ω_6 values trend is the same as the studied glasses in Refs. [60,61,63,65,67,69] in Table 4. Recently, for different RE ions doped phosphors or nanocrystals also, J–O parameters have been derived and reported by researchers utilizing the excitation spectra [71], luminescence spectra and radiative transition lifetimes [72], diffuse-reflection spectra [73], and through fluorescence decay routes [74].

Intending to reckon fluorescence qualities of all A–F samples, radiative factors such as A_{ed}, A_{md}, A_R (=A_{ed} + A_{md}), β_R, and τ_R for optical transitions (SLJ → S'L'J') from Tm^{3+}: $^1D_2$, $^1G_4$, $^3F_2$, $^3F_3$, $^3H_4$, $^3H_5$ and $^3F_4$ excited levels are calculated applying related J–O parameters and

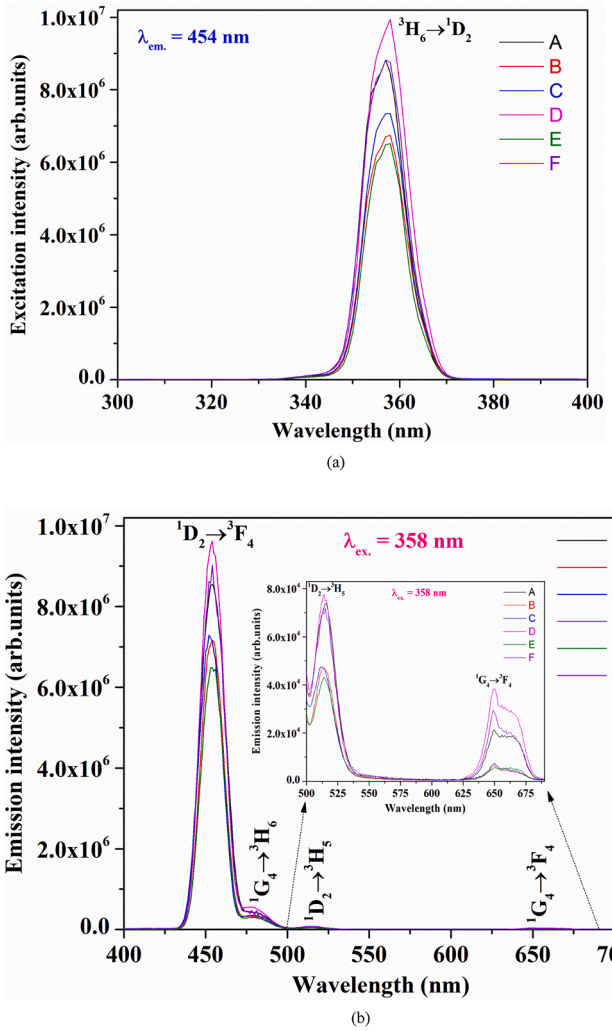

Fig. 4. (a) Photoluminescence excitation (PLE) spectra of all the 1.0 mol% Tm^{3+}-doped glasses by monitoring emission at 454 nm (b) Photoluminescence (PL) spectra (inset, within the 500–690 nm range) of all the 1.0 mol% Tm^{3+}-doped glasses under 358 nm excitation wavelength.

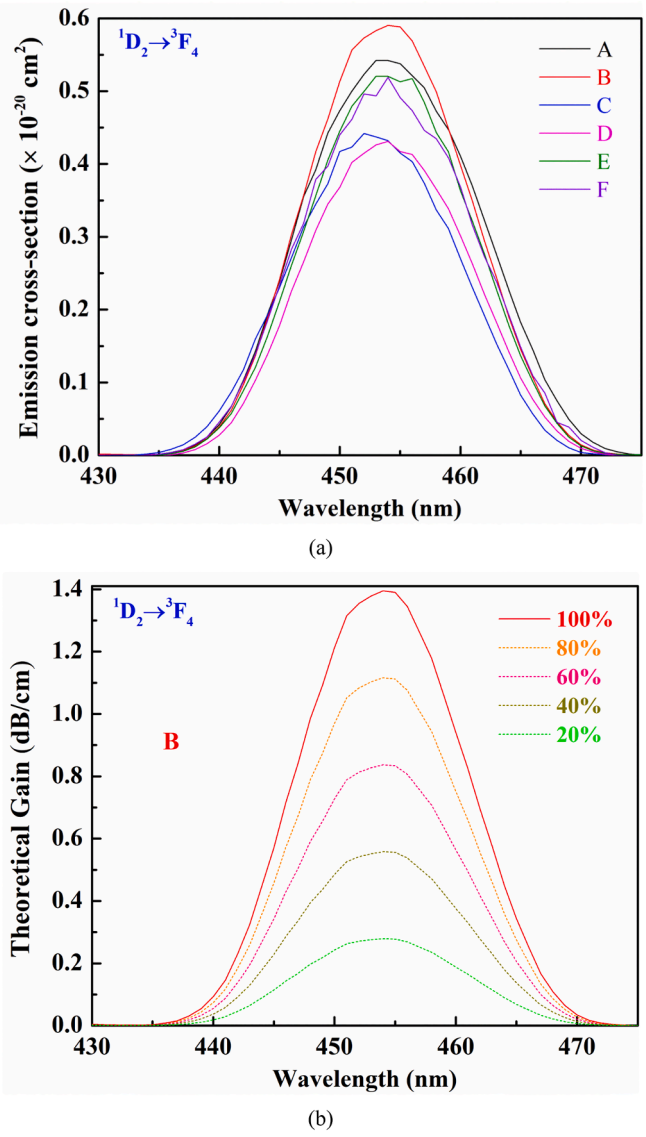

Fig. 5. (a) Stimulated emission cross-section profiles of the $^1D_2 \rightarrow {}^3F_4$ transition of all the A–F glasses (b) Predicted theoretical gain spectra of the $^1D_2 \rightarrow {}^3F_4$ transition of glass B.

refractive indices and attained results are given in Table 5 for glass B and for remaining all glasses in Table S1 (i–v) in Supplementary material accordingly. For all these radiative features computations, applied familiar formulae can be found elsewhere [28,31,32,36]. Glass B has relatively high A_R (=4825 s^{-1}) and moderate β_R (=22.92%) for $^1D_2 \rightarrow {}^3F_4$ transition which indicates its ascendancy for blue lasing action in all A–F samples. Likewise, sample A possesses the largest A_R (=103 s^{-1}) in all glasses for $^3H_4 \rightarrow {}^3F_4$ transition suggesting its fairer capacity for ~ 1.46 μm optical amplification. Interestingly all A–F glasses have β_R = 100% for $^3F_4 \rightarrow {}^3H_6$ laser transition where glass C has the highest τ_R (=7.737 ms) as commonly longer τ_R is favorable to decrease laser threshold. Further τ_R for Tm^{3+}: $^1D_2 \rightarrow {}^3F_4$ transition in glass B (=47.5 μs) is found to be greater than the respective values of BBLC 1.0Tm (=0.0002 ms) [61], KCaAlP: Tm^{3+} (=37.83 μs) [69], and PKSATm10 (=27 μs) [70] glasses and lower than $LiKB_4O_7$: Tm (=53 μs) [28] glass and almost equal to $Li_2B_4O_7$: Tm,Ag glass (=48 μs) [31].

Visible photoluminescence and decay lifetime analyses

Fig. 4(a) exhibits optical excitation spectra for all A–F glasses within 300–400 nm spectral range recorded at 454 nm fluorescence wavelength. An intense excitation band peaked at 358 nm is identified from all samples which could be ascribed to the transition from $^3H_6$ level to $^1D_2$ state [70]. Registered visible luminescence spectra for all A–F samples at 400–720 nm wavelength region under 358 nm (representing to $^1D_2$ state) pumping are displayed in Fig. 4(b) while the corresponding inset plot shows the zoom-in wavelength range at 500–690 nm. All samples emission features appear the same in shape and have four bands: two in blue ($^1D_2 \rightarrow {}^3F_4$ and $^1G_4 \rightarrow {}^3H_6$), one in green ($^1D_2 \rightarrow {}^3H_5$), and another in red ($^1G_4 \rightarrow {}^3F_4$) regions that are peaked at 454 nm, 479 nm, 514 nm, and 650 nm accordingly [28]. Commonly, for Tm^{3+}-doped materials, upper excited states $^1D_2$ and $^1G_4$ lead to fluorescence in the visible wavelength range whereas lower $^3F_4$ and $^3H_4$ excited levels cause NIR emissions. Here $^1G_4 \rightarrow {}^3H_6$, $^1D_2 \rightarrow {}^3H_5$, and $^1G_4 \rightarrow {}^3F_4$ emission transitions are so weak compared to $^1D_2 \rightarrow {}^3F_4$ luminescence transition intensity as blue emission centered at 454 nm is highly intense. In all glasses, for observed four bands, sample D shows relatively higher fluorescence intensity correlating to its excitation one (see Fig. 4). Normally overlapped 4f orbitals with ligands split Tm^{3+} ion's energy levels causing degenerate states and any change in network structure could, in turn, affects Tm^{3+} ion's emission and absorption cross-sections.

Next, for all A–F glasses, to realize identified $^1D_2 \rightarrow {}^3F_4$ blue fluorescence transition qualitatively, by scaling Fig. 4(b) we determined

Table 6
Radiative lifetime (τ_{rad}, μs), effective bandwidth ($\Delta\lambda_{eff}$, nm), stimulated peak emission cross-section ($\sigma^{em}_{max} \times 10^{-21}$ cm^2), gain bandwidth ($\sigma^{em}_{max} \times \Delta\lambda_{eff} \times 10^{-27}$ cm^3), optical gain ($\sigma^{em}_{max} \times \tau_{rad} \times 10^{-25}$ cm^{2}s), and Branching ratio (β_R,%) of the $^1D_2 \rightarrow {}^3F_4$ transition for all the A–F glasses.

Sample code	τ_{rad}	$\Delta\lambda_{eff}$	σ^{em}_{max}	$\sigma^{em}_{max} \times \Delta\lambda_{eff}$	$\sigma^{em}_{max} \times \tau_{rad}$	β_R
A	44.33	17.738	5.42	9.614	2.403	21.23
B	47.50	16.452	5.89	9.69	2.798	22.92
C	65.13	16.773	4.41	7.397	2.872	24.92
D	62.87	16.500	4.29	7.078	2.697	22.28
E	55.07	16.615	5.19	8.623	2.858	24.23
F	51.52	16.789	5.17	8.68	2.663	22.52

Table 7
CIE 1931 color coordinates (x, y), dominant wavelength (λ_d), dominant wavelength color coordinates (x_d, y_d), color purity (CP), luminous efficiency of radiation (LER) and emission color for all A–F glasses excited at 358 nm wavelength.

Sample code	CIE (x, y)	λ_d (nm)	(x_d, y_d)	CP (%)	LER (lm/W)	Emission color
A	(0.1489, 0.0298)	457	(0.1458, 0.0229)	97.8	40.7	Purplish-blue
B	(0.1496, 0.0285)	458	(0.1478, 0.0285)	99.7	39.2	Purplish-blue
C	(0.1507, 0.0275)	458	(0.1505, 0.0270)	99.8	38.0	Purplish-blue
D	(0.1491, 0.0295)	459	(0.1482, 0.0262)	99.0	40.3	Purplish-blue
E	(0.1495, 0.0288)	459	(0.1482, 0.0295)	100.0	39.6	Purplish-blue
F	(0.1494, 0.0294)	460	(0.1482, 0.0285)	99.6	40.2	Purplish-blue

stimulated emission cross-section (σ_{em}) (for operating lasers and fiber amplifiers with better gain and energy extraction rate, a large σ_{em} is essential) applying the Füchtbauer–Ladenburg equation [67,68]:

$$\sigma_{em}(\lambda) = \frac{A_{ij}}{8\pi cn^2} \times \frac{\lambda^5 \boldsymbol{I}(\lambda)}{\int \lambda \boldsymbol{I}(\lambda) d\lambda} \quad (7)$$

where c, n, A_{ij}, and $\boldsymbol{I}(\lambda)$ correspond to light speed, refractive index, spontaneous emission probability, and fluorescence intensity at λ (wavelength) from $i \rightarrow j$ level separately.

Derived σ_{em} curves of all A–F samples for $^1D_2 \rightarrow {}^3F_4$ transition at 430–475 nm spectral range are depicted in Fig. 5(a) and from them, evaluated peak σ_{em} (σ^{em}_{max}) values are given in Table 6.

Also, effective bandwidths ($\Delta\lambda_{eff}$) for 454 nm peak emission band are obtained by a relation [69]:

$$\Delta\lambda eff = \frac{1}{I_{max}} \int \boldsymbol{I}(\lambda) d\lambda$$

where I_{max} = intensity at band maximum, $I(\lambda)$ = intensity at λ.

Acquired $\Delta\lambda_{eff}$ values for all A–F glasses are listed in Table 6.

Moreover, peak gain bandwidth ($\sigma^{em}_{max} \times \Delta\lambda_{eff}$) and optical gain ($\sigma^{em}_{max} \times \tau_{rad}$) are computed and presented in Table 6 along with τ_{rad} and β_R for all studied samples.

Here, typically $\sigma_{em} \times \Delta\lambda_{eff}$ and $\sigma_{em} \times \tau_{rad}$ results are useful in inspecting the optical amplification and laser threshold of a RE ion-doped medium. From Table 6 it is clear that Tm^{3+}: Na ions containing glass (sample B) shows the highest σ^{em}_{max} (=5.89 × 10^{-21} cm^2) and $\sigma^{em}_{max} \times \Delta\lambda_{eff}$ (=9.69 × 10^{-27} cm^3) values for $^1D_2 \rightarrow {}^3F_4$ transition in all samples, indicating its favorability for *cw* blue lasing process with a fine gain.

Later utilizing σ_{em} and β_R, with an expectation that $^1D_2$ upper state is fully (100%) or partly (80%, 60%, 40%, and 20%) populated by Tm^{3+} ions under 358 nm pumping, for all A–F samples the theoretical gain for 454 nm centered luminescence band is assessed utilizing the relevant formula [75]:

$$G(\lambda, P) = 10 \log_{10} \exp(PN\beta\sigma_{em}(\lambda)) \quad (9)$$

where P = excited Tm^{3+} ions' fractional factor in $^1D_2$ state, N = total Tm^{3+} ion concentration.

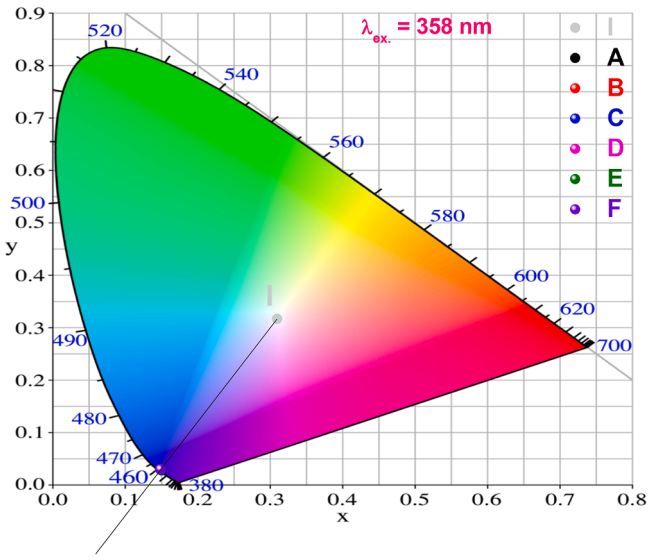

Fig. 6. 1931 CIE color chromaticity coordinates diagram for all the 1.0 mol% Tm^{3+}-doped single and mixed alkali oxides containing glasses under 358 nm excitation wavelength.

Fig. 5(b) exhibits estimated theoretical gain spectra of $^1D_2 \rightarrow {}^3F_4$ transition at 430–475 nm region for glass B and for remaining all samples obtained gain spectra are presented in Supplementary material (see Fig. S1(a–e)). From Fig. 5(b) and Fig. S1 in Supplementary material, one can notice that $G(\lambda, P)$ is improved constantly with ions population density (P) increment from 0.2 to 1.0. Sample B possesses the maximal $G(\lambda, P)$ (=1.395 dB/cm) value in all samples when the $^1D_2$ level is 100% populated. Also at P = 0.6, the $G(\lambda, P)$ at 0.454 μm is 0.835 dB/cm for glass B.

To recognize the total visible fluorescence of all A–F samples, corresponding CIE chromaticity coordinates (x, y) are determined from Fig. 4(b) applying color functions $\bar{x}(\lambda)$, $\bar{y}(\lambda)$, and $\bar{z}(\lambda)$ and related values are listed in Table 7. Also, Fig. 6 depicts the 2-D CIE chromaticity diagram for all A–F glasses under λ_{ex} = 358 nm. All A–F samples display an overall tonality within the purplish-blue region with a dominant wavelength in the 457–460 nm range (see Table 7). The CIE1931 chromaticity coordinates are close to those reported for blue illumination by the National Television System Committee (NTSC) (x = 0.140, y = 0.080) and European Broadcasting Union (EBU) (x = 0.150, y = 0.060) [76].

Later, CIE coordinates values are utilized to evaluate percent CP values for all A–F glasses utilizing the following relation [43]:

$$CP = \sqrt{\frac{(x - x_i)^2 + (y - y_i)^2}{(x_d - x_i)^2 + (y_d - y_i)^2}} \times 100\% \quad (10)$$

where (xi, yi) = (0.310, 0.316) = CIE1931 Standard Source I illuminate point coordinates, (x_d, y_d) = dominant wavelength coordinates, (x, y) = sample point coordinates.

Obtained percent CP values are given in Table 7 and they are better than those reported for Tm^{3+}-doped zinc phosphate glasses (96%) [77], Tm^{3+}: $CaAl_4O_7$ (73%) [78], and Tm^{3+}: $CaBi_2B_2O_7$ (97%) [79] phosphors, and similar to those of reported for Tm^{3+}: $Ca_9NaGd_{2/3}(PO_4)_7$ phosphors (96.8–99.1%) [80]. This fact points out that all studied A–F samples might be suitable to develop a blue-emitting source upon near-UV excitation (358 nm), especially glass E. Further for all A–F samples, LER values are computed using NIST CQS simulation 7.4 following the approach given in Refs. [81,82] and are tabulated in Table 7, and these values are varied at 38–40.7 lm/W range.

For obtaining additional details on luminescence qualities of all A–F

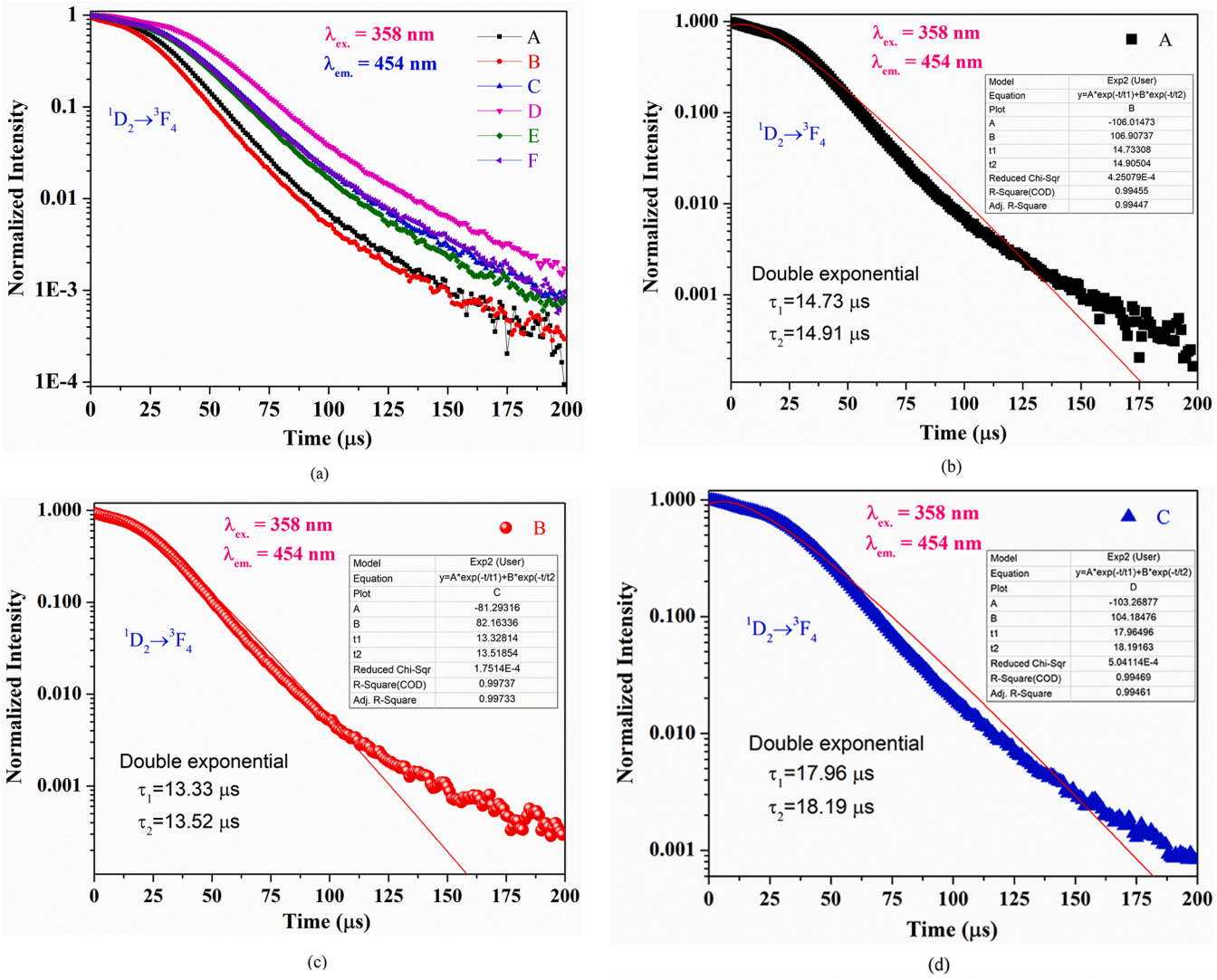

Fig. 7. (a) Decay lifetime profiles of the Tm^{3+}: $^1D_2 \rightarrow {}^3F_4$ transition for all A–F glasses under 358 nm excitation wavelength (b–f) Decay lifetime profiles fit of the Tm^{3+}: $^1D_2 \rightarrow {}^3F_4$ transition for all A–F glasses.

glasses, Tm^{3+}: $^1D_2$ state decay time patterns are studied under $\lambda_{ex.} = 358$ nm for 454 nm fluorescence band. Fig. 7(a) shows $^1D_2 \rightarrow {}^3F_4$ transition decay curves for all A–F samples. Here $^1D_2$ level decay profiles of all A–F glasses are well fit to double-exponential functions (Adj. R-Square = 0.9925–0.9973)

as [21]:

$I(t) = A\exp(\frac{-t}{\tau_1}) + B\exp(\frac{-t}{\tau_2})$, (11)where $I(t)$ = fluorescence intensity, A and B = constants, t = time, and τ_1 andτ_2 = rapid and slow emission decay times.

Fig. 7(b–g) illustrates decay time profiles fit of Tm^{3+}: $^1D_2 \rightarrow {}^3F_4$ transition for all respective A–F samples and derived average lifetimes (τ_{meas}) are given in Table 5 and Table S1 (i – v) in Supplementary material respectively. Glass D has the largest τ_{meas} (=33.37 μs) in all samples for $^1D_2 \rightarrow {}^3F_4$ transition. From Table 5 and Table S1, it is clear that τ_{rad} is higher than τ_{meas} because of larger NR relaxations from $^1D_2$ to its lower-lying states.

For all A–F samples quantum efficiency (η) for $^1D_2$ level of Tm^{3+} in the visible spectral region is calculated by the well-known formula:

$\eta = \frac{\tau_{meas}}{\tau_{rad}} \times 100\%$ (12)

Commonly 'η' of a fluorescence state banks on its σ_{em}, A_R, τ_{exp}, and RE ion concentration doping levels. For all A–F glasses derived η values are listed in Table 5 and Table S1 (i – v) in Supplementary material accordingly. In all glasses, sample F possesses high 'η' (=55%). Also for all A–F samples, 'η' for $^1D_2$ state is greater than those of $LiKB_4O_7$:Tm (η = 26.4%) [28] and $Li_2B_4O_7$:Tm (η = 32.1%) [31] glasses and lower than that of $Li_2B_4O_7$:Tm,Ag (η = 64.6%) [31] glass reported values.

NIR luminescence analysis

Fig. 8 exhibits NIR fluorescence spectra of all A–F samples within 1300–1600 nm range under 808 nm LD pumping. As expected, a wide asymmetric NIR emission band centered at 1463 nm is identified from all glasses which can be attributed to Tm^{3+}: $^3H_4 \rightarrow {}^3F_4$ transition [4,5]. Owing to utilized detector sensitivity maximal constraint, NIR luminescence was registered up to 1600 nm wavelength only, so $^3F_4 \rightarrow {}^3H_6$ (~1.8 μm) NIR emission transition has not fully observed. In all glasses, sample B shows the largest emission intensity for the $^3H_4 \rightarrow {}^3F_4$ transition. Interestingly one can see from Fig. 8 that NIR luminescence spectra become wider and expand to longer spectral regions forming shoulder bands when respective Na_2O and K_2O replace Li_2O in the glass composition. Here Na_2O and K_2O could improve the host-ion ligand's ionic nature leading to increased field strength than Li_2O and as a result, $^3H_4 \rightarrow {}^3F_4$ transition shows Stark splittings enhancing NIR emissions broadening further [83]. So by optimizing a glass composition one can

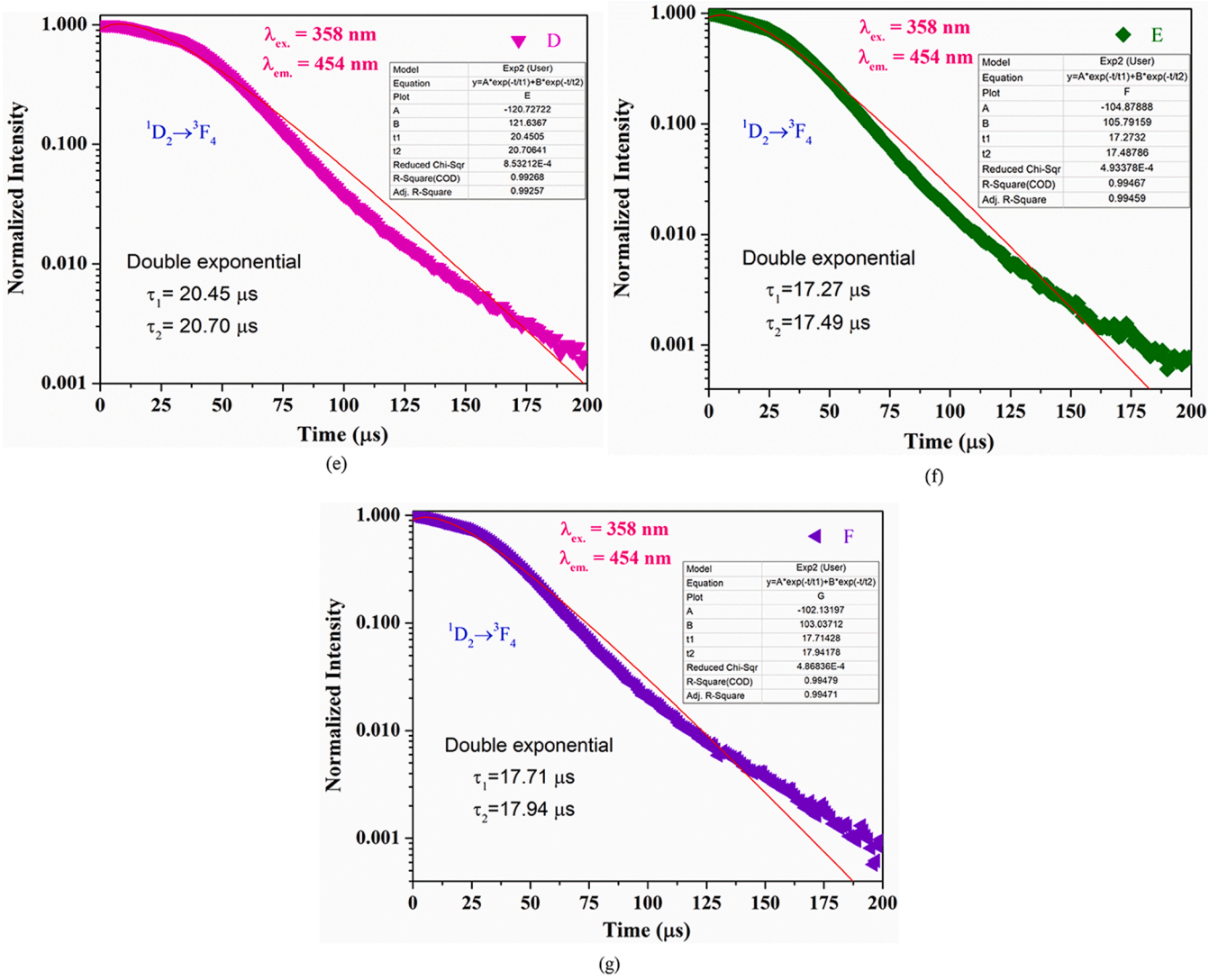

Fig. 7. (*continued*).

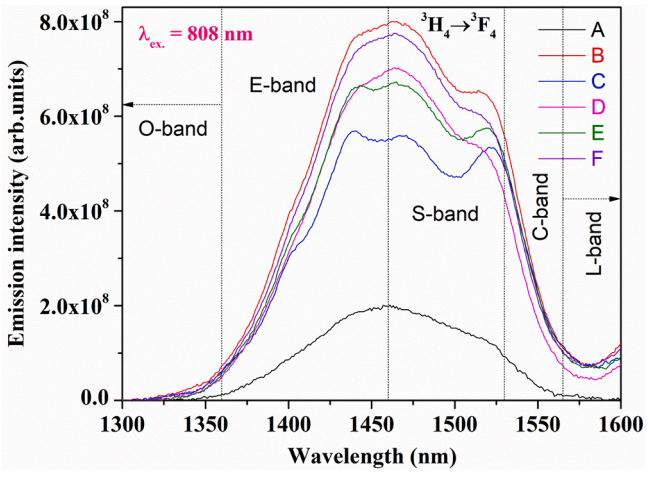

Fig. 8. NIR luminescence spectra of all the 1.0 mol% Tm^{3+}-doped glasses upon 808 nm LD excitation.

get much overlap between C- and S-optical bands for multichannel propagation. As can be seen from Fig. 8, the $^3H_4 \rightarrow {}^3F_4$ transition is extending from 1.36 μm to 1.565 μm wrapping E-+S-+C-optical bands for amplification as it is required to design Tm^{3+}-doped media with wide $\Delta\lambda_{eff}$ for optical WDM communication systems. As 1.463 μm NIR emission from $^3H_4$ level is productive when it is directly excited, it could be speculated that sufficient Tm^{3+} ion population at $^3H_4$ state could be obtained under 808 nm LD excitation at 1 mol% doping. Generally, because of CR (cross-relaxation) which is a NR ET (energy transfer) process, 1.46 μm fluorescence reduces and 1.8 μm emission enhances in intensity at relatively larger Tm^{3+} doping contents by depleting Tm^{3+} ions population at $^3H_4$ state and increasing them at $^3F_4$ level [67].

Utilizing Eq. (7) mentioned previously, by scaling the NIR fluorescence spectra at measured 1300–1600 nm spectral range, σ_{em} of $^3H_4 \rightarrow {}^3F_4$ transition is assessed for all A–F glasses and related σ_{em} profiles are illustrated in Fig. 9(a). Deduced peak σ_{em} (σ^{em}_{max}) values at 1.46 μm for all studied glasses are listed in Table 8. Also, evaluated respective $\Delta\lambda_{eff}$ values for all A–F samples are presented in Table 8 with τ_{rad} values for $^3H_4 \rightarrow {}^3F_4$ transition. In all glasses, sample A has the largestσ^{em}_{max} (=1.832 × 10–^{21} cm^2) correlating to its highest A_R. Moreover, evaluated σ_{abs} (absorption cross-section) ($= \frac{\alpha(\lambda)}{N_{Tm^{3+}}}$) values of $^3H_6 \rightarrow {}^3H_4$ and $^3H_6 \rightarrow {}^3F_4$ transitions for all A–F samples are (1.68, 1.65, 1.34, 1.26, 1.52, and 1.48) × 10^{-20} cm^2 and (9.43, 8.75, 5.89, 6.58, 7.30, and 7.93) × 10^{-21} cm^2 accordingly where glass A possesses the highest σ_{abs} for the NIR optical pumping. Further one can notice from Table 8 that in single alkali oxides containing glasses from A to C sample $\Delta\lambda_{eff}$ increased

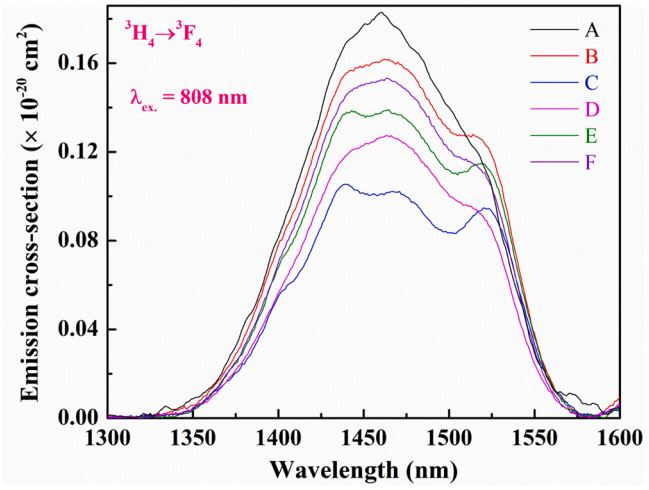

(a)

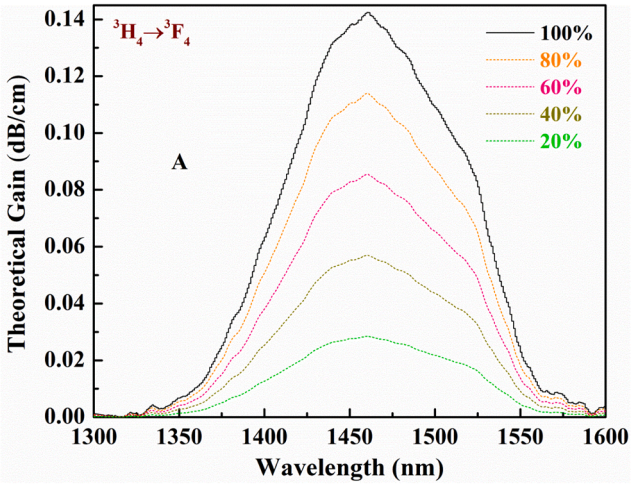

(b)

Fig. 9. (a) Stimulated emission cross-section profiles of the $^3H_4 \rightarrow {}^3F_4$ transition for all A–F glasses (b) Predicted theoretical gain spectra of the $^3H_4 \rightarrow {}^3F_4$ transition for glass A.

Table 8
Radiative lifetime (τ_{rad}, μs), effective bandwidth ($\Delta\lambda_{eff}$, nm), stimulated peak emission cross-section ($\sigma^{em}_{max} \times 10^{-21}$ cm^2), gain bandwidth ($\sigma^{em}_{max} \times \Delta\lambda_{eff} \times 10^{-26}$ cm^3), and optical gain ($\sigma^{em}_{max} \times \tau_{rad} \times 10^{-25}$ cm^{2}s) of the $^3H_4 \rightarrow {}^3F_4$ transition for all the A–F glasses.

Sample code	τ_{rad}	$\Delta\lambda_{eff}$	σ^{em}_{max}	$\sigma^{em}_{max} \times \Delta\lambda_{eff}$	$\sigma^{em}_{max} \times \tau_{rad}$
A	688.23	121.228	1.832	2.22	12.608
B	703.73	130.801	1.617	2.115	11.379
C	890.29	137.638	1.055	1.452	9.392
D	914.51	125.463	1.27	1.593	11.614
E	773.84	133.316	1.387	1.849	10.733
F	763.87	126.596	1.532	1.939	11.702

continuously from 121.228 nm to 137.638 nm whereas in mixed alkali oxides having samples $\Delta\lambda_{eff}$ improved considerably for Na-K ions existence in the glass compared to Li-Na or Li-K ions. These changes in $\Delta\lambda_{eff}$ and σ^{em}_{max} in all examined glasses suggest a notable effect of changing alkali oxides on existed Tm^{3+} ions environment. Next, using σ^{em}_{max}, $\Delta\lambda_{eff}$, and τ_{rad}, both $\sigma^{em}_{max} \times \Delta\lambda_{eff}$ and $\sigma^{em}_{max} \times \tau_{rad}$ values are derived for all A–F glasses to understand the chances of high gain amplification with wideband ($^3H_4 \rightarrow {}^3F_4$), and obtained results are tabulated in Table 8. Here glass A with largest σ^{em}_{max}, $\sigma^{em}_{max} \times \Delta\lambda_{eff}$, and $\sigma^{em}_{max} \times \tau_{rad}$ values specify

Table 9
Comparison of effective bandwidth ($\Delta\lambda_{eff}$, nm), emission peak cross-section ($\sigma^{em}_{max} \times 10^{-21}$ cm^2), and gain bandwidth ($\sigma^{em}_{max} \times \Delta\lambda_{eff} \times 10^{-26}$ cm^3) of $^3H_4 \rightarrow {}^3F_4$ emission transition for different Tm^{3+}-doped glass systems.

Glass system	$\Delta\lambda_{eff}$	σ^{em}_{max}	$\sigma^{em}_{max} \times \Delta\lambda_{eff}$	Reference
Glass A	121.228	1.832	2.22	Present work
1 mol% Tm^{3+}: ZBLAN glass	76	1.8	1.368	[84]
0.5 mol%: 75TeO_2:10ZnO:15Na_2O glass	114	3.6	4.104	
0.2 wt% Tm_2O_3-doped LKBBG glass	122	3.34	4.07	[85]
Tm^{3+}: TeO_2-WO_3-PbO (TWP20) glass	102	4	4.08	[86]
1 mol% Tm^{3+}: 60Bi_2O_3–20SiO_2-20Ga_2O_3-1.5$AgNO_3$ glass	128	4.8	6.14	[4]
Tm^{3+}-doped KCaAlP glass	125.21	2.37	2.967	[69]
Tm^{3+}: P_2O_5 + K_2O + SrO + Al_2O_3 glass	120	3.37	4.04	[70]

the chances of effective amplification within identified wide spectral range. Further glass A $\Delta\lambda_{eff}$, σ^{em}_{max}, and$\sigma^{em}_{max} \times \Delta\lambda_{eff}$ values of $^3H_4 \rightarrow {}^3F_4$ transition are compared with reported some other Tm^{3+}-doped glasses [4,69,70,84–86] (see Table 9). One can see from Table 9 that sample A has higher $\Delta\lambda_{eff}$ than those of Tm^{3+}: P_2O_5 + K_2O + SrO + Al_2O_3 [70], 1 mol% Tm^{3+}: ZBLAN and 0.5 mol%: 75TeO_2: 10ZnO: 15Na_2O [84], and TWP20 [86] glasses respective values and it is almost equal to 0.2 wt% Tm_2O_3-doped LKBBG glass [85]. Likewise, glass A possesses largerσ^{em}_{max} and$\sigma^{em}_{max} \times \Delta\lambda_{eff}$ values than 1 mol% Tm^{3+}: ZBLAN glass [84] related values and lower than remaining other glasses in comparison. Here, by Tm^{3+} doping content optimization, σ^{em}_{max} and$\sigma^{em}_{max} \times \Delta\lambda_{eff}$ values could be possibly enhanced further for glass A. Moreover, RE ions' σ_{em} enhances with host refractive index (n) increment as σ_{em} α $(n^2 + 2)^2/n$ for ED transitions and σ_{em} α n for MD transitions, so a glass matrix with a high 'n' is desirable for acquiring a large σ_{em} for NIR optical amplification [87].

Later for all A–F samples, utilizing Eq. (9) at P = 0.2, 0.4, 0.6, 0.8, and 1.0, the theoretical gain of $^3H_4 \rightarrow {}^3F_4$ transition within 1.3–1.6 μm range is computed and as an example, Fig. 9(b) depicts gain spectra for sample A where for rest of the glasses derived gain profiles are displayed in Fig. S2(a–e) in Supplementary material. Glass A exhibits the highest $G(\lambda, P)$ (=0.142 dB/cm) value in all glasses when the $^3H_4$ state is 100% populated. Also at P = 0.6, the $G(\lambda, P)$ at 1.46 μm is 0.085 dB/cm for sample A. Here, while gain spectra cover E-+S-+C-bands, both E- and C-bands necessitate principally a strong pumping to acquire lasing activity. Usually, for wideband multimodal fiber amplifiers to operate at 1.45–1.58 μm range with enhanced SNR (signal-to-noise ratio), TDFA gain spectra leading edge must have to overlap with EDFA gain profiles trailing end which essentially needs Tm^{3+} NIR emission peaked at 1.46 or 1.47 μm and gain pattern to move to longer NIR wavelengths covering C-band mostly [83]. Commonly, larger gain bandwidths lower WDM systems overall cost as a single fiber amplifier could be utilized to amplify all communicating channels.

Fig. 10 depicts Tm^{3+} ion's energy-level diagram for all A–F samples upon both 358 nm UV excitation and 808 nm LD pumping showing all identified visible and NIR luminescence transitions and relevant NR process and CR channels of $^1D_2$ and $^3H_4$ upper levels. Upon 358 nm pumping, initially, Tm^{3+} ions in $^3H_6$ ground state are excited to $^1D_2$ level. For all A–F glasses, τ_{rad} values of $^1D_2$ state which are varied within 44.33–65.13 μs range are lower than the next lower-lying $^1G_4$ state (varied at 324.41– 446.11 μs range, see Table 5 and Table S1 in Supplementary material). So from the $^1D_2$ state, a large number of Tm^{3+} ions will rapidly deexcite radiatively to $^3F_4$ level emitting intense blue light (454 nm) and a weak green emission by relaxing to $^3H_5$ state (514 nm). Here ($^1D_2$, $^3H_6$)→($^3F_2$, $^3H_4$) and ($^1D_2$, $^3H_6$)→($^3F_3$,$^3F_3$) are the feasible CR channels for $^1D_2 \rightarrow {}^3F_4$ transition. Residual Tm^{3+} ions in $^1D_2$ level will depopulate *via* NR process to $^1G_4$ level, then, they finally

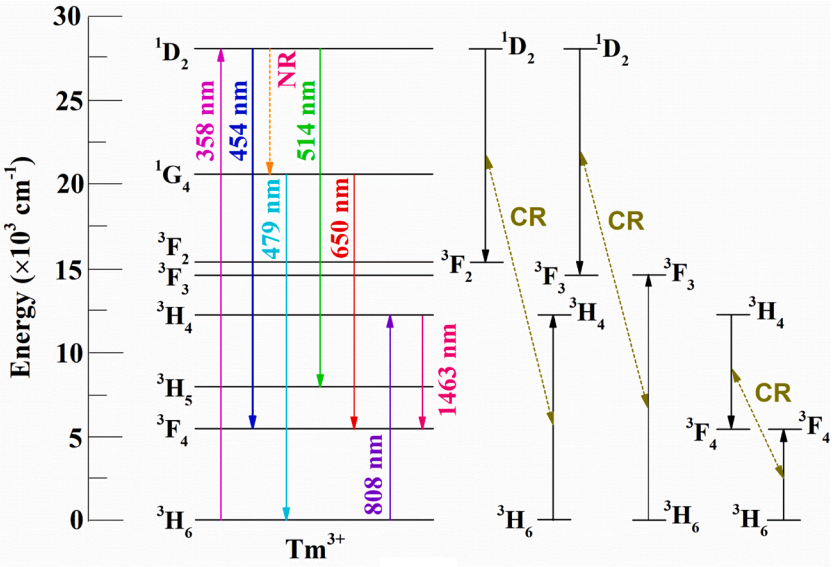

Fig. 10. Partial energy-level diagram of the Tm^{3+} ion for the studied glasses, depicting the UV and NIR excitations, and visible and NIR emission transitions, including CR channels for $^1D_2$ and $^3H_4$ excited levels.

radiatively deexcite to $^3H_6$ and $^3F_4$ states causing weak blue and red fluorescences (479 nm and 650 nm) accordingly. Likewise, under 808 nm LD excitation, first, Tm^{3+} ions in $^3H_6$ state are promoted to $^3H_4$ level. Later a considerable fraction of Tm^{3+} ions will radiatively relax to $^3F_4$ state giving NIR emission peaked at 1.463 μm. Though the CR ET process ($^3H_4$+$^3H_6$→$^3F_4$+$^3F_4$) adversely affects the population of Tm^{3+} ions at the $^3H_4$ level it is advantageous in acquiring intense NIR fluorescence radiative transition ($^3F_4$→$^3H_6$) centered at 1.8 μm owing to the existing high energy gap (~6,000 cm^{-1}) between $^3F_4$ and $^3H_6$ states. In glasses, generally doping lower Tm^{3+} ion contents are favorable for S-band amplifiers usage, and appropriate large Tm^{3+} concentrations are desirable for designing 1.8 μm NIR lasers [85].

Conclusions

Six transparent Tm^{3+}-doped (1 mol%) B_2O_3-BaO-ZnO-LiF glasses having single and mixed alkali oxides as Li_2O (A), Na_2O (B), and K_2O (C), and Li_2O-Na_2O (D), Na_2O-K_2O (E), and Li_2O-K_2O (F) sequentially were prepared by the melt-quenching route. All these glasses were characterized by optical absorption, Vis-NIR luminescence and decay times, and analyzed. From UV absorption spectra, λ_{edge}, E_{opt}, and Urbach energies (ΔE) were estimated where E_{opt} and ΔE relied on NBOs number and all A–F samples have larger ΔE values (0.39–0.508 eV range) suggesting maximal defects or disorders in their amorphous structure. Applying J–O theory, $\Omega_2 > \Omega_4 > \Omega_6$ trend for A, B, D, and F glasses, and $\Omega_2 > \Omega_6 > \Omega_4$ and $\Omega_2 > \Omega_6 > \Omega_4$ courses for C and E samples accordingly were derived with fewer δ_{rms} deviations (good least-squares fit) between f_{exp} and f_{cal}. For sample B, evaluated larger Ω_2 signifies a lower symmetry at Tm^{3+} ion sites locality and high covalency between Tm^{3+} and O^{2-} ions. Ω_λ ($\lambda = 2, 4, 6$) parameters were used to compute A_R, β_R, and τ_R of Tm^{3+} ion's all emitting levels in A–F glasses. Glass B has relatively large A_R (=4825 s^{-1}) and moderate β_R (=22.92%) for $^1D_2$→$^3F_4$ transition for effective blue lasing action. Upon 358 nm pumping, four visible luminescence bands centered at 454 nm, 479 nm, 514 nm, and 650 nm respectively were observed, and in them, blue emission ($^1D_2$→$^3F_4$) dominates for all A–F glasses. In all samples, glass B has the highest σ^{em}_{max} (=5.89 × 10^{-21} cm^2) andσ^{em}_{max} × $\Delta\lambda_{eff}$ (=9.69 × 10^{-27} cm^3), and maximal $G(\lambda, P)$ (=1.395 dB/cm at $P = 1$) value for $^1D_2$→$^3F_4$ transition to utilizing it as an active medium for blue lasers and high-density optical data storage devices application. $^1D_2$ excited state decay curves of all A–F glasses were fitted well using double-exponential function. Under λ_{ex} = 358 nm, all A–F glasses' CIE coordinates were located in the purplish-blue region, and deduced high CP (%) values are varied at 97.8–100 range. In all A–F samples, a broad asymmetric NIR fluorescence band centered at 1463 nm ($^3H_4$→$^3F_4$ transition) was noticed upon 808 nm LD excitation as 1.46 μm emission is highly essential since it is the next minimal loss communication window to Er^{3+} ion's NIR (~1.55 μm) luminescence. The obtained variations in $\Delta\lambda_{eff}$ and σ^{em}_{max} of $^3H_4$→$^3F_4$ transition indicated a considerable effect of changing alkali oxides on the Tm^{3+} ions' environment in the glass matrix. Considering $^3H_4$→$^3F_4$ transition, although A–F glasses have lower σ^{em}_{max} values, $\Delta\lambda_{eff}$ values are considerably higher than those of Tm^{3+}: tellurite glasses, and σ^{em}_{max} for sample A is larger than that of fluoride (Tm^{3+}: ZBLAN) glass value. Wide $\Delta\lambda_{eff}$ (=121 nm) (covering entire S-optical band), large σ^{em}_{max} (=1.832 × 10^{-21} cm^2), high(σ^{em}_{max} × $\Delta\lambda_{eff}$) (=2.22 × 10^{-26} cm^3), large σ^{em}_{max} × τ_{rad} (=12.608 × 10^{-25} cm^2s), and $G(\lambda, P)$ = 0.085 dB/cm at P = 0.6 for $^3H_4$→$^3F_4$ transition in glass A specifies its potential as a medium for wideband amplification application in WDM optical systems.

CRediT authorship contribution statement

G. Lakshminarayana: Conceptualization, Methodology, Visualization, Writing - original draft, Writing - review & editing, Supervision. **A. N. Meza-Rocha:** Investigation, Data curation, Validation. **O. Soriano-Romero:** Investigation. **E.F. Huerta:** Formal analysis, Visualization. **U. Caldiño:** Investigation, Data curation, Validation. **A. Lira:** Formal analysis, Data curation. **Dong-Eun Lee:** Resources, Project administration, Funding acquisition, Supervision. **Jonghun Yoon:** Resources, Supervision. **Taejoon Park:** Resources, Project administration, Funding acquisition, Supervision.

Declaration of Competing Interest

The authors declare that they have no known competing financial interests or personal relationships that could have appeared to influence the work reported in this paper.

Acknowledgements

This work was supported by the National Research Foundation of Korea (NRF) grant funded by the Korea government (MSIT) (No. NRF-2018R1A5A1025137) and the Korea Institute of Energy Technology

Evaluation and Planning (KETEP) and the Ministry of Trade, Industry & Energy (MOTIE), Korea (No. 20172010105470).

Appendix A. Supplementary data

Supplementary data to this article can be found online at https://doi.org/10.1016/j.rinp.2021.104343.

References

[1] Richardson K, Krol D, Hirao K. Glasses for photonic applications. Int J Appl Glass Sci 2010;1:74–86.

[2] DeCorby R, Irannejad M. Glasses for photonic integration. In: Kasap S, Capper P, editors. Springer handbook of electronic and photonic materials. Springer handbooks. Cham: Springer; 2017. https://doi.org/10.1007/978-3-319-48933-9_41.

[3] Nishimura S, Fuchi S, Takeda Y. Luminescence properties of Tm_2O_3-doped oxide glasses for NIR wideband light source. J Mater Sci: Mater Electron 2017;28(10):7157–62.

[4] Meng S, Zhao G, Hou J, Liu Y, Guo Y, Fang Y, et al. High performance of near-infrared emission for S-band amplifier from Tm^{3+}-doped bismuth glass incorporated with Ag nanoparticles. J Lumin 2020;224:117313.

[5] Yang G, Zhang Q, Shi D, Jiang Z. Tm^{3+}-doped gallium–germanium–bismuth–lead glasses as 1.47 μm fiber amplifier materials. J Am Ceram Soc 2007;90:307–10.

[6] Muravyev SV, Anashkina EA, Andrianov AV, Dorofeev VV, Motorin SE, Koptev MY, et al. Dual-band Tm^{3+}-doped tellurite fiber amplifier and laser at 1.9 μm and 2.3 μm. Sci Rep 2018;8:16164/1-13.

[7] Wang P, Yi Y, Wang X, Li A, Jia S, Fan Y, et al. Tm^{3+}-doped fluorotellurite glass microsphere resonator laser at 2.3 μm. Opt Lett 2020;45:3553–6.

[8] Shixun D, Bo P, Pengjun Z, Tiefeng Xu, Wang X, Qiuhua N, et al. The near- and mid-infrared emission properties of Tm^{3+}-doped GeGaS–CsI chalcogenide glasses. J Non-Cryst Solids 2010;356(44-49):2424–8.

[9] Ebrahim-Zadeh M, Sorokina IT. Mid-Infrared Coherent Sources and Applications. Physics and Biophysics) (Springer: NATO Science for Peace and Security Series B; 2007.

[10] Kaur P, Singh K, Devra S, Kaur G, Singh ML. Evaluation of gain spectrum of silica-based single/dual-pumped thulium-doped fiber amplifier (TDFA) by optimizing its physical and pumping parameters in the scenario of dense wavelength division multiplexed systems (DWDM). J Opt Commun 2019;40:353–62.

[11] .S.-H. Yam, M.E. Marhic, T. Sakamoto, E.S.-T. Hu, Y. Akasaka, L.G. Kazovsky, Comparison of four wave mixing and cross phase modulation in thulium doped fiber amplifier and S-band discrete Raman amplifier, in Proc. OECC, Yokohama, Japan. (2002). pp. 9D1–9D4.

[12] M.H. Aly, M. Nasr, H.E. Seleem, Thulium doped fiber amplifier in the S/S+ band employing different concentration profiles, Fifth Workshop on Photonics and its Applications, Giza, Egypt. (2005). pp. 39–49.

[13] Shen X, Zhu Y, Zhou Y, Li J. Broadband and flat near-infrared emission from Er^{3+}/Tm^{3+} codoped tellurite glass for amplifier applications. J Opt Soc Am B 2020;37(2):320. https://doi.org/10.1364/JOSAB.379743.

[14] Li J, Wang X, Yang H, Jiang Z. Ultraviolet upconversion emission from ZBLAN glass doped with Tm^{3+} ions. Phys B: Condens Matter 2007;392:251–4.

[15] Trindade CM, Alves RT, Gouveia-Neto AS. Tunable reddish to magenta upconversion luminescence in Tm^{3+}-doped glass. Opt Eng 2018;57:097104.

[16] Li J, Wang X, Jiang Z. Multiphoton upconversion process in Tm^{3+} doped ZBLAN glass by CW laser irradiation. Opt Commun 2009;282(21):4249–51.

[17] Gouveia-Neto AS, Vermelho MVD, Gouveia EA, Bueno LA, Jacinto C. .319 μm excited intense 800 nm frequency upconversion emission in Tm3+-doped fluorogermanate glass. Appl Phys Lett 2015;107. 211103/1–4.

[18] Praveena R, Jang KH, Jayasankar CK, Seo HJ. Optical absorption and fluorescence properties of Tm^{3+}-doped K-Mg–Al phosphate glasses for laser applications. J Alloy Compd 2010;496(1-2):335–40.

[19] Xu R, Xu L, Hu L, Zhang J. Structural origin and laser performance of thulium-doped germanate glasses. J Phys Chem A 2011;115(49):14163–7.

[20] Yang H, Gao J. Different dynamics of ultraviolet upconversion in Tm^{3+}:ZBLAN glass under blue laser excitation. Phys B: Condens Matter 2013;426:31–4.

[21] Shestakov MV, Chen XM, Kaydashev V, Baeckelant W, Tikhomirov VK, Vanacken J, et al. Oxyfluoride glass (SiO_2-PbF_2) co-doped with Ag nanoclusters and Tm^{3+} ions for UV-driven, Hg-free, white light generation with a tuneable tint. Opt Mater Express 2014;4:1227–35.

[22] Gebavi H, Taccheo S, Milanese D. The enhanced two micron emission in thulium doped tellurite glasses. Opt Mater 2013;35(10):1792–6.

[23] Denker BI, Dorofeev VV, Galagan BI, Koltashev VV, Motorin SE, Plotnichenko VG, et al. 2.3 μm laser action in Tm^{3+}-doped tellurite glass fiber. Laser Phys Lett 2019;16:015101/1-4.

[24] Xu W, Chen D, Yan Q, Ren J, Chen G. Silver metal enhanced photoluminescence of Tm^{3+} doped GeS_2–Ga_2S_3–CsCl glasses. J Non-Cryst Solids 2012;358(23):3065–8.

[25] Galstyan A, Messaddeq SH, Fortin V, Skripachev I, Vallée R, Galstian T, et al. Tm^{3+} doped Ga–As–S chalcogenide glasses and fibers. Opt Mater 2015;47:518–23.

[26] Lee Y-W, Chien H-W, Cho C-H, Chen J-Z, Chang J-S, Jiang S. Heavily Tm^{3+} -doped silicate fiber for high-gain fiber amplifiers. Fibers 2013;1(3):82–92.

[27] Cao R, Lu Yu, Tian Y, Huang F, Guo Y, Xu S, et al. Mid-infrared luminescence and energy transfer of Tm^{3+} in silicate glasses by codoping with Yb^{3+} ions. Opt Laser Technol 2017;94:106–11.

[28] Kindrat II, Padlyak BV, Lisiecki R, Adamiv VT. Optical spectroscopy and luminescence properties of a Tm^{3+}-doped $LiKB_4O_7$ glass. J Non-Cryst Solids 2019;521:119477.

[29] Kozak MM, Goebel D, Caspary R, Kowalsky W. Spectroscopic properties of thulium-doped zirconium fluoride and indium fluoride glasses. J Non-Cryst Solids 2005;351(24-26):2009–21.

[30] Chen H, Liu Y-H, Yao X-X, Feng Z-M. Effect of Tm^{3+}-doping concentration on the spectral properties in tellurite glass. Acta Phys Sinica 2005;54:4427–32.

[31] Kindrat II, Padlyak BV, Lisiecki R, Adamiv VT. Spectroscopic and luminescent properties of the lithium tetraborate glass co-doped with Tm and Ag. J Lumin 2020;225:117357.

[32] Satyanarayana T, Kityk IV, Brik MG, Kumar VR, Veeraiah N. Fluorescence features of Tm^{3+} ions in PbO–Sb_2O_3–B_2O_3 glass ceramics. Phys B: Condens Matter 2010;405:1872–80.

[33] Xu Z, Chen Y, Lin Y, Gong X, Luo Z, Huang Y. Effect of concentration on the spectral properties of Tm^{3+} ions in bismuth borate glasses. J Alloy Compd 2009;481(1-2):411–6.

[34] Liu X, Chen G, Chen Y, Xu J. Luminescent properties and energy transfer of Tm^{3+}/Dy^{3+} co-doped oxyfluoride borate glasses for white LEDs. J Mater Sci: Mater Electron 2018;29(18):16041–9.

[35] Venkateswarlu M, Swapna K, Mahamuda Sk, Rani PR, Kumar JVS, Prasad MVVKS, Rao AS. Concentration dependent neodymium doped oxy fluoroborate glasses for 1.08 μm laser applications. Solid State Sci 2021;113:106543.

[36] Yasukevich AS, Rachkovskaya GE, Zakharevich GB, Trusova EE, Kornienko AA, Dunina EB, et al. Spectral-luminescence properties of oxyfluoride lead-silicate-germanate glass doped with Tm^{3+} ions. J Lumin 2021;229:117667.

[37] Feng Li, Wu Yinsu, Liu Zhuo, Guo Tao. Optical transitions of Tm^{3+} in oxyfluoride glasses and compositional and thermal effect on upconversion luminescence of Tm^{3+}/Yb^{3+}-codoped oxyfluoride glasses. Spectrochim Acta-A: Mol Biomol Spectrosc 2014;118:192–8.

[38] de Pablos-Martin A, Patzig C, Höche T, Duran A, Pascual MJ. Distribution of thulium in Tm^{3+}-doped oxyfluoride glasses and glass-ceramics. CrystEngComm 2013;15(35):6979. https://doi.org/10.1039/c3ce40731d.

[39] Mishra RK, Sudarsan V, Kaushik CP, Raj Kanwar, Kulshreshtha SK, Tyagi AK. Effect of BaO addition on the structural aspects and thermophysical properties of sodium borosilicate glasses. J Non-Cryst Solids 2007;353(16-17):1612–7.

[40] Masuda H, Kimura R, Sakamoto N, Morinaga K. Properties and structure of glasses in the system BaO-B_2O_3-ZnO. J Jpn Inst Met 1999;63:284–8.

[41] Lakshminarayana G, Kaky KM, Baki SO, Lira A, Nayar P, Kityk IV, et al. Physical, structural, thermal, and optical spectroscopy studies of TeO_2–B_2O_3–MoO_3–ZnO–R_2O (R = Li, Na, and K)/MO (M = Mg, Ca, and Pb) glasses. J Alloy Compd 2017;690:799–816.

[42] Zheng L-L, Wu T-Z, Lu Y-J, Gao Y-L, Wang Y-J, Zhu L-H, Guo Z-Q, Chen Z. Spectral optimization of three-primary LEDs by considering the circadian action factor. IEEE Photon J 2016;8. 8200209/1–9.

[43] Huerta EF, Meza-Rocha AN, Lozada-Morales R, Speghini A, Bordignon S, Caldiño U. White, yellow and reddish-orange light generation in lithium-aluminum-zinc phosphate glasses co-doped with Dy^{3+}/Tb^{3+} and tri-doped with Dy^{3+}/Tb^{3+}/Eu^{3+}. J Lumin 2020;219:116882.

[44] Carnall WT, Fields PR, Wybourne BG. Spectral intensities of the trivalent lanthanides and actinides in solution. I. Pr^{3+}, Nd^{3+}, Er^{3+}, Tm^{3+}, and Yb^{3+}. J Chem Phys 1965;42(11):3797–806.

[45] Ibrahim S, ElBatal FH, Abdelghany AM. Optical character enrichment of NdF_3 -doped lithium fluoroborate glasses. J Non-Cryst Solids 2016;453:16–22.

[46] ElBatal FH, Ibrahim S, Abdelghany AM. Optical and FTIR spectra of NdF_3-doped borophosphate glasses and effect of gamma irradiation. J Mol Struct 2012;1030:107–12.

[47] Bougradja F, Diaf M, Fartas R, Boubekri H, Khiari S. Photoluminescence investigations of Tm^{3+} doped SrF_2 single crystals for visible and infrared laser applications. Opt Mater 2020;108:110143.

[48] Wang R, Zhang J, Zhang Y, Lin H, Pun EY-B, Li D. Phosphor-in-glass with full-visible-spectrum emission based on ultra-low melting Sn-F-P-O glass pumped by NUV LED chips. J Alloy Compd 2021;864:158671.

[49] Mott NF, Davis EA. Electronic processes in non-crystalline materials. 2nd ed. Oxford, UK: Clarendon Press; 1979.

[50] Tauc J. In: Amorphous and liquid semiconductors. Boston, MA: Springer US; 1974. p. 159–220. https://doi.org/10.1007/978-1-4615-8705-7_4.

[51] Escobar-Alarcón L, Arrieta A, Camps E, Muhl S, Rodil S, Vigueras-Santiago E. An alternative procedure for the determination of the optical band gap and thickness of amorphous carbon nitride thin films. Appl Surf Sci 2007;254(1):412–5.

[52] Souri D, Shomalian K. Band gap determination by absorption spectrum fitting method (ASF) and structural properties of different compositions of (60–x) V_2O_5-40TeO_2-xSb_2O_3 glasses. J Non-Cryst Solids 2009;355:1597–601.

[53] Mallur Saisudha B, Czarnecki Tyler, Adhikari Ashish, Babu Panakkattu K. Compositional dependence of optical band gap and refractive index in lead and bismuth borate glasses. Mater Res Bull 2015;68:27–34.

[54] Urbach F. The long-wavelength edge of photographic sensitivity and of the electronic absorption of solids. Phys Rev 1953;92:1324.

[55] Abdel-Baki M, Abdel-Wahab FA, El-Diasty F. One-photon band gap engineering of borate glass doped with ZnO for photonics applications. J Appl Phys 2012;111.073506/1–10.

[56] Mizrahi Victor, Saifi MA, Andrejco MJ, DeLong KW, Stegeman GI. Two-photon absorption as a limitation to all-optical switching. Opt Lett 1989;14(20):1140. https://doi.org/10.1364/OL.14.001140.

[57] Judd BR. Optical absorption intensities of rare-earth ions. Phys Rev 1962;127(3):750–61.

[58] Ofelt GS. Intensities of crystal spectra of rare-earth ions. J Chem Phys 1962;37(3):511–20.
[59] Jørgensen Christian K, Reisfeld Renata. Judd-Ofelt parameters and chemical bonding. J Less Common Met 1983;93(1):107–12.
[60] Tu L, Tang G, Qian Q, Yang Z. Controllable structural tailoring for enhanced ~2 μm emission in heavily Tm^{3+}-doped germanate glasses. Opt Lett 2021;46:310–3.
[61] El-Maaref AA, Wahab EA Abdel, Shaaban KhS, Abdelawwad M, Koubisy MSI, Börcsök J, et al. Visible and mid-infrared spectral emissions and radiative rates calculations of Tm^{3+} doped BBLC glass. Spectrochim Acta-A: Mol Biomol Spectrosc 2020;242:118774. https://doi.org/10.1016/j.saa.2020.118774.
[62] Song X, Han K, Zhou D, Xu P, Xue X, Zhang P. ~2 μm emission properties and energy transfer processes in Tm^{3+} doped Bi_2O_3-GeO_2-Na_2O glass laser material. J Lumin 2020;224:117314.
[63] Basavapoornima Ch, Maheswari T, Deviprasad CJ, Kesavulu CR, Tröster Th, Jayasankar CK. Thermal, structural, mechanical and 1.8 μm luminescence properties of the thulium doped Pb-K-Al-Na glasses for optical fiber amplifiers. J Non-Cryst Solids 2020;530:119773.
[64] Qi Fangwei, Huang Feifei, Lei Ruoshan, Tian Ying, Zhang Long, Zhang Junjie, et al. Emission properties of 1.8 and 2.3 μm in Tm^{3+}-doped fluoride glass. Glass Phys Chem 2017;43(4):340–6.
[65] Doualan JL, Girard S, Haquin H, Adam JL, Montagne J. Spectroscopic properties and laser emission of Tm doped ZBLAN glass at 1.8 μm. Opt Mater 2003;24(3):563–74.
[66] Marzuki A, Riyatun M, Larasati GT Singgih. Radiative properties of Tm^{3+} doped TeO_2-ZnO-Na_2O-TiO_2 glasses studied using Judd-Ofelt Theory. IOP Conf Ser: Mater Sci Eng 2019;675:012070/1-6.
[67] Gao S, Liu X, Fan X, Li X, Xue T, Li K, Liao M, Hu L. ~2 μm emission properties and non-radiative processes of Tm3+ in germanate glass. J Appl Phys 2014;116.173108/1–6.
[68] Cankaya H, Gorgulu AT, Kurt A, Speghini A, Bettinelli M, Sennaroglu A. Comparative spectroscopic investigation of Tm^{3+}: tellurite glasses for 2-μm lasing applications. Appl Sci 2018;8. 333/1–10.
[69] Kermaoui A, Pellé F. Synthesis and infrared spectroscopic properties of Tm^{3+}-doped phosphate glasses. J Alloy Compd 2009;469(1-2):601–8.
[70] Linganna K, Kumar KU, Jayasankar CK. Spectroscopy and 1.47 μm emission properties of Tm^{3+}-doped metaphosphate laser glasses. Mat Express 2013;3:71–8.
[71] Luo Wenqin, Liao Jinsheng, Li Renfu, Chen Xueyuan. Determination of Judd-Ofelt intensity parameters from the excitation spectra for rare-earth doped luminescent materials. PCCP 2010;12(13):3276. https://doi.org/10.1039/b921581f.
[72] Tian Yue, Chen Baojiu, Hua Ruinian, Sun Jiashi, Cheng Lihong, Zhong Haiyang, et al. Optical transition, electron-phonon coupling and fluorescent quenching of $La_2(MoO_4)_3$:Eu^{3+} phosphor. J Appl Phys 2011;109(5):053511. https://doi.org/10.1063/1.3551584.
[73] Zhang Y, Chen B, Xu S, Li X, Zhang J, Sun J, et al. A universal approach for calculating the Judd-Ofelt parameters of RE^{3+} in powdered phosphors and its application for the β-$NaYF_4$:Er^{3+}/Yb^{3+} phosphor derived from auto-combustion-assisted fluoridation. PCCP 2018;20:15876–83.
[74] Luo Mengyan, Chen Baojiu, Li Xiangping, Zhang Jinsu, Xu Sai, Zhang Xizhen, et al. Fluorescence decay route of optical transition calculation for trivalent rare earth ions and its application for Er^{3+}-doped $NaYF_4$ phosphor. PCCP 2020;22(43):25177–83.
[75] Lakshminarayana G, Kaky Kawa M, Baki SO, Lira A, Meza-Rocha AN, Falcony C, et al. Nd^{3+}-doped heavy metal oxide based multicomponent borate glasses for 1.06 μm solid-state NIR laser and O-band optical amplification applications. Opt Mater 2018;78:142–59.
[76] Han B, Zhang J, Li PJ, Shi HZ. $KBaBP_2O_8$:Tm^{3+}: a novel blue-emitting phosphor with high color purity. JETP Lett 2014;99:561–4.
[77] Meza-Rocha AN, Speghini A, Lozada-Morales R, Caldiño U. Blue and white light emission in Tm^{3+} and Tm^{3+}/Dy^{3+} doped zinc phosphate glasses upon UV light excitation. Opt Mater 2016;58:183–7.
[78] Kumar A Suresh, Kumar R Arun, Bhattacharjee Rama Ranjan. Synthesis and optical characterization of Tm^{3+} doped $CaAl_4O_7$ for near–UV LED–based white light. J Lumin 2017;182:130–6.
[79] Li J, Yan H, Yan F. A novel high color purity blue-emitting phosphor: $CaBi_2B_2O_7$:Tm^{3+}. Mater Sci Eng, B 2016;209:56–9.
[80] Deng B, Chen J, Zhou C-song, Liu H. Blue-emitting Tm^{3+}-doped $Ca_9NaGd_{2/3}(PO_4)_7$ phosphor with excellent thermal stability. Optik 2020;202:163658.
[81] Y. Ohno, Color rendering and luminous efficacy of white LED spectra, Fourth International Conference on Solid State Lighting, (eds. I.T. Ferguson, N. Narendran, S.P. DenBaars, J.C. Carrano), Proc. SPIE 5530 (2004) 88–98.
[82] Ohno Y. Spectral design considerations for white LED color rendering. Opt Eng 2005;44. 111302/1–9.
[83] Shen S, Jha A, Wilson SJ, Zhang E. The effect of composition on the emission spectra of Tm^{3+}-doped tellurite glasses for an S-band amplifier operating at 1.46 μm. J Non-Cryst Solids 2003;326-327:510–4.
[84] Naftaly M, Shen S, Jha A. Tm^{3+}-doped tellurite glass for a broadband amplifier at 1.47 μm. Appl Opt 2000;39:4979–84.
[85] Lin H, Wang XY, Li CM, Yang HX, Pun EYB, Tanabe S. Near-infrared emissions and quantum efficiencies in Tm^{3+}-doped heavy metal gallate glasses for S- and U-band amplifiers and 1.8 μm infrared laser. J Lumin 2008;128(1):74–80.
[86] Balda R, Lacha LM, Fernández J, Arriandiaga MA, Fernández- Navarro JM, Munoz-Martin D. Spectroscopic properties of the 1.4 μm emission of Tm^{3+} ions in TeO_2-WO_3-PbO glasses. Opt Express 2008;16:11836–46.
[87] R. Reisfeld, C.K. Jørgensen, Rare-Earth Lasers. In: Lasers and Excited States of Rare Earths. Inorganic Chemistry Concepts, vol 1. Springer, Berlin, Heidelberg. (1997). Chap. 2, pp. 64–122.